Development of Ramsey Interferometry-based Imaging with Ultracold Atoms

A thesis submitted in partial fulfillment of the requirement
for the degree of Bachelor of Science with Honors in
Physics from the College of William and Mary in Virginia,

by

Yiyang Ding

Advisor: Prof. Seth Aubin

Prof. Saskia Mordijck

Prof. Ashley Gao

Williamsburg, Virginia
April 17 2026

Contents

Acknowledgments **iv**

List of Figures **vii**

Abstract **v**

1 Introduction **1**

1.1 Motivation 1

1.2 Overall Structure 4

2 Theory **5**

2.1 Brief Introduction of Rb 87 Hyperfine Structure 5

2.2 Rabi Oscillation 7

2.3 AC Stark Shift 10

2.4 Scattering Rate 11

2.5 Scenarios for Imaging External Field with Rb-87 in MOT chamber . . 12

2.5.1 Imaging a laser beam 12

2.5.2 Imaging an electron beam 15

2.6 Adiabatic Rapid Passage 16

2.7 Ramsey Interferometry 16

2.8 Spin Echo 21

3 Experimental Apparatus **24**

3.1 Brief Overview of Ultracold Atom Apparatus 24

3.2 Microwave System 25

3.3 Imaging System 30

3.3.1 Imaging System on the Atom Chip 30

3.3.2 Imaging System in the MOT Region 32

4 Methodology and Results **34**

4.1 Ramsey Interferometry under Atom Chip 34

4.1.1 Atom Chip Trap 34

4.1.2 Microwave operation 35

4.1.3 Rabi flopping and Ramsey Interferometry results 37

4.1.4 Atomic state Population Ratio Noise 41

4.2 Ramsey Interferometry Process in the MOT for imaging a laser beam 43

4.2.1 Evaporation cooling 44

4.2.2 Resonance scans of microwave transitions and corresponding Rabi flopping 45

4.2.3 Ramsey interferometry 52

4.2.4 Prospects for Ramsey interferometry-based imaging a laser beam 54

5 Conclusion **55**

A **57**

A.1 The atom cloud structure during a resonance scan under a magnetic gradient 57

A.2 Pre-works for imaging a laser beam 59

A.3 New version of fluorescence imaging system 59

References **59**

Acknowledgments

I would first like to thank my family for their unwavering support throughout my growth and undergraduate journey. I am also deeply grateful to my friends for bringing happiness and joy into my life.

Next, I would like to thank my group members—Russell Kamback, William Miyahira, Trevor Tingle, and Adam Vernon—for their patience and support. Whether helping me understand the apparatus and the underlying atomic physics or assisting with technical issues during the experiments, they have all contributed greatly to this work. The progress described in this thesis is the result of a collaborative group effort, and it would not have been possible without them.

I would also like to thank Prof. Eugeniy Mikhailov and Irina Novikova for inspiring my interest in quantum physics. In addition, I am grateful to Prof. Saskia Mordijck and Prof. Ashley Gao for serving on my honors thesis committee.

Finally, I would like to express my deepest gratitude to my advisor, Prof. Seth Aubin, for his patience, time, and guidance since my sophomore year. He has helped me develop a deep understanding of both the project and the related physics, and he has continually supported me in overcoming experimental challenges with thoughtful advice and encouragement.

List of Figures

1.1 Two-level atom scenario for imaging a laser beam 2

1.2 Two-level atom scenario for imaging an electron beam 3

2.1 Rb-87 D2 line hyperfine structure 6

2.2 Zeeman Splitting on Rb-87 hyperfine levels 7

2.3 A two-level atom system will a driving field and Rabi oscillation . . . 9

2.4 Rabi Oscillation on Bloch sphere 10

2.5 AC Stark shift 11

2.6 Imaging a laser beam using cold Rb-87 atoms in the MOT chamber . 13

2.7 The relationship between energy shifts or scattering rate with laser detuning 14

2.8 Imaging an electron beam using cold Rb-87 atoms in the MOT chamber 15

2.9 Adiabatic Rapid Passage 17

2.10 Ramsey Interferometry and Rabi Flopping on the Bloch Sphere . . . 18

2.11 Stimulated Ramsey fringes and shifts due to the laser field 20

2.12 Spin Echo Operation Sequence 22

2.13 Stimulated Spin echo fringes. 23

3.1 Main ultracold atom apparatus 25

3.2 Logic diagram of our microwave system 26

3.3 Microwave system components 27

3.4 Logic diagram of IQ-Modulator 28
3.5 Full picture of IQ-Modulator based microwave system for generating around $2\pi\times$ 3.4 GHz microwave field 29
3.6 Laser pulse diagram for imaging atoms on the atom chip 31
3.7 Imaging System Setup for MOT Region 33
3.8 The Rb-87 atom cloud in the MOT 33

4.1 The DC magnetic trap on the atom chip 35
4.2 The hyperfine levels and Zeeman sublevels of Rb-87 36
4.3 $|2,2>$ to $|1,1>$ resonance frequency scan 37
4.4 Atomic states demonstration with Stern-Gerlach field on CCD 38
4.5 Adiabatic Rapid Passage for atomic state manipulations 39
4.6 $|2,0>$ to $|1,0>$ on-resonance Rabi flopping 39
4.7 Ramsey Interferometry between $|2,0>$ and $|1,0>$ states 40
4.8 Atomic noise comparison (laser-power and camera-gain optimization) 41
4.9 Atomic noise comparison (magnetic sensitivity) 42
4.10 Fluorescence imaging result on the atom chip 42
4.11 The atom cloud with an unknown magnetic gradient 43
4.12 Visualize Evaporation Cooling by Atom Cloud image 45
4.13 Thermal expansion rate of an atom cloud after the evaporation cooling 46
4.14 $|2,2>$ to $|1,1>$ resonance scan under 7.5 G vertical bias field in the MOT region 46
4.15 $|2,2>$ and $|1,1>$ states Rabi flopping in the MOT region 48
4.16 Adiabatic Rapid Passage from $|2,2>$ and $|1,1>$ states in MOT region 49
4.17 $|1,1>$ to $|2,0>$ resonance scan under 7.5 G bias field in the MOT region 49

4.18 $|1,1>$ to $|2,0>$ Rabi flopping with on resonance frequency under 7.5 G bias field in the MOT region 50
4.19 Adiabatic Rapid Passage from $|1,1>$ and $|2,0>$ states in the MOT region 50
4.20 $|1,1>$ to $|2,0>$ resonance frequency scan 51
4.21 $|2,0>$ to $|1,0>$ Rabi flopping under 7.5 G bias field in the MOT region 51
4.22 Ramsey Interferometry between $|2,0>$ and $|1,0>$ states 53

A.1 Atom cloud structures during the resonance scan under the effect of an unknown external magnetic gradient 58
A.2 AOM-based laser shutter 59
A.3 New version of fluorescence imaging system 60

Abstract

This thesis describes all work on developing Ramsey Interferometry at the atom chip region, including building the IQ-Modulator microwave system, the imaging system, and quantum-state control using microwave fields. Ramsey Interferometry in the atom chip region during the atoms' free fall between the $|2,0>$ and $|1,0>$ states has an approximate coherent time of 4ms. Also, we work towards the development of Ramsey Interferometry in the MOT chamber to image the laser beam, which we developed Evaporation Cooling to minimize the effects of the magnetic gradient in the environment, built a new imaging system, and strategies (i.e., two cloud imaging in one picture) to collect data, and performed Ramsey Interferometry.

Chapter 1

Introduction

This introductory chapter describes the short-term objectives of this experimental research project and its long-term motivation, summarizes my work, and provides guidelines for reading or using this thesis.

1.1 Motivation

The primary objective of my research project is to develop and implement a non-invasive method for imaging a laser beam and eventually an electron beam. People may be curious why we need a new way to image a laser beam. Lasers are "visible," so why not just look at them or point a camera at them? In many routine situations, conventional detectors are the right tool, but they have limits in certain practical situations. In particular, high-power beams can permanently damage the optics, filters, or pixels of a sensor. Additionally, placing any sensor directly in the beam blocks the laser light, which is unacceptable if the beam must continue downstream to perform useful work. Our approach is to image the beam using a cloud of atoms — i.e., a cold-atom "dust" — that can non-invasively probe it without absorbing or stopping it. Of course, setting up a weak pick-off beam is an easier way to probe, but it usually adds extra noise to the measurement. More specifically, our approach measures the spectroscopic shift of atomic energy levels induced by the laser's electric

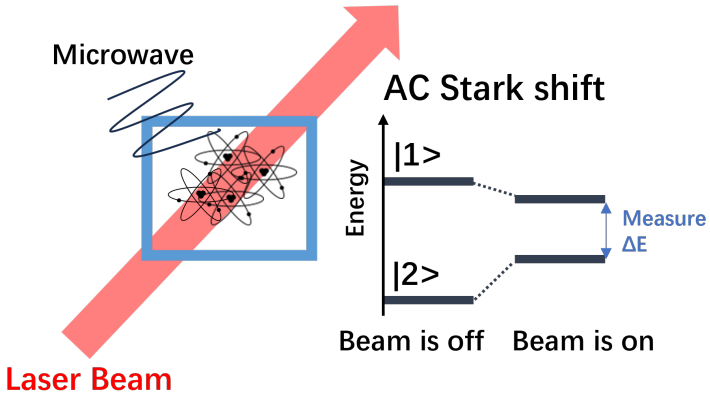

Figure 1.1: This figure illustrates the two-level scenario in which atoms interact with a laser beam. The microwave is used for coupling the two states $|1>$ and $|2>$ in the atoms.

field and can be extended to measure the electric field of an electron beam.

Moving on to the real experiment, the biggest question is: how can we utilize atoms in reality? In the lab, we put rubidium atoms into the vacuum chamber, where they exist as a thermal gas. We use a magneto-optical trap (MOT) to trap and cool the atoms in a small region – people can really see the atom cloud in the apparatus! Then the atoms can either be well prepared for the experiment in the MOT chamber or transported to the atom chip region. Naturally, atoms can have different states representing the same energy. We apply a magnetic field to separate the states and distinguish them. For a more straightforward interpretation, imagine that you open Google Maps and, once you enter a destination, it shows several routes to that place. At this point, there will be energy or frequency differences between the states, and by applying a frequency with the proper value and intensity, we can enable two states to communicate. Then, if we allow a laser beam to pass through the atomic clouds, the two states will experience energy shifts (i.e., the AC Stark shift). In other words, we can gain information about the laser beam (or electron beam) by measuring how much the states shift (Figure 1.1).

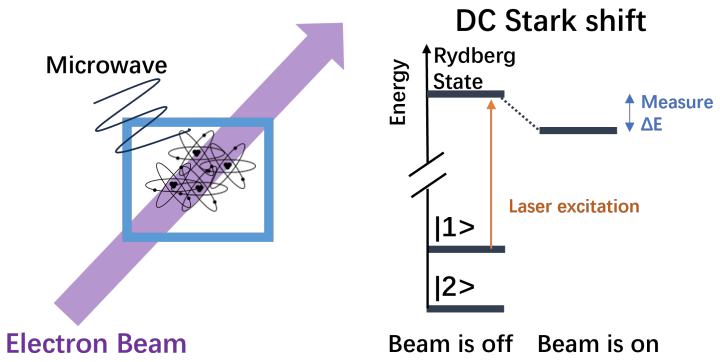

Figure 1.2: This figure illustrates the two-level scenario in which atoms interact with an electron beam. The microwave is used to couple the two states $|1>$ and $|2>$ in the atoms, and then two lasers (or three lasers) are used to excite the atoms to the Rydberg state for electric- or magnetic-field sensing.

In the real experiment, Ramsey Interferometry, which involves two brief microwave pulses applied to the atoms, is very helpful for measuring small, temporary energy-level shifts. If we do Ramsey Interferometry without a laser beam, the result will be an oscillating signal between two states, whereas with a laser beam, the signal will have a phase shift relative to the original Ramsey signal. By measuring the phase shift, we can indirectly know how much energy shift there is. Currently, most of my work focuses on imaging a laser beam in the MOT chamber and on developing Ramsey interferometry on the atom chip.

Ultimately, our final goal is to use a similar technique to image an electron beam, optimally a single electron. However, we need photons to excite the atoms from ground states to the Rydberg state, which is more sensitive to the electric field (Figure 1.2). The related sensing techniques can be used to enhance particle detection of electrons, protons, and muons at Jefferson Lab [1] [2] [3].

1.2 Overall Structure

This thesis is organized in the following manner: Chapter 2 reviews the theoretical concepts used in the experiment and also provides general numerical calculations used in designing the experiment. Chapter 3 covers the experimental apparatus and introduces the hardware systems and instruments we use during the experiment, providing a general sense of how the experiment is conducted. Chapter 4 describes the main experimental results, including diagrams, plots, and related data analysis. Chapter 5 concludes by providing an outlook for future research directions based on the work.

Chapter 2

Theory

This chapter reviews the basic physics underlying the measurement and imaging of the electric field of a laser beam. Sections 2.1, 2.2, and 2.3 review the basic physics of the formulas for the AC Stark shifts in a two-level atom and the scattering rate for a laser. Section 2.4 calculates the expected AC Stark Shifts and associated laser scattering rate for the proposed experiment. Finally, sections 2.5, 2.6, and 2.7 review the microwave state manipulation techniques of adiabatic rapid passage, Ramsey interferometry, and Spin Echo. To ensure unit consistency, all frequencies are expressed as angular frequencies.

2.1 Brief Introduction of Rb 87 Hyperfine Structure

Rubidium is in the group of alkali atoms, which have one valence electron. The hyperfine structure of Rb-87 is defined by the L, S, J, and F quantum numbers, with $|L-S| \leq J \leq L+S$ and $|J-I| \leq F \leq J+I$. The nuclear angular momentum number(I) of Rb-87 is $I = \frac{3}{2}$, the electron spin angular momentum number (S) is $S = \frac{1}{2}$, and the electron orbital angular momentum number (L) is determined by which orbit the outer electron is at. In our experiment, we focus on the D2 line on the $5S_{\frac{1}{2}} \leftrightarrow 5P_{\frac{3}{2}}$ (J=$\frac{3}{2}$ for the first excited state), and the corresponding hyperfine

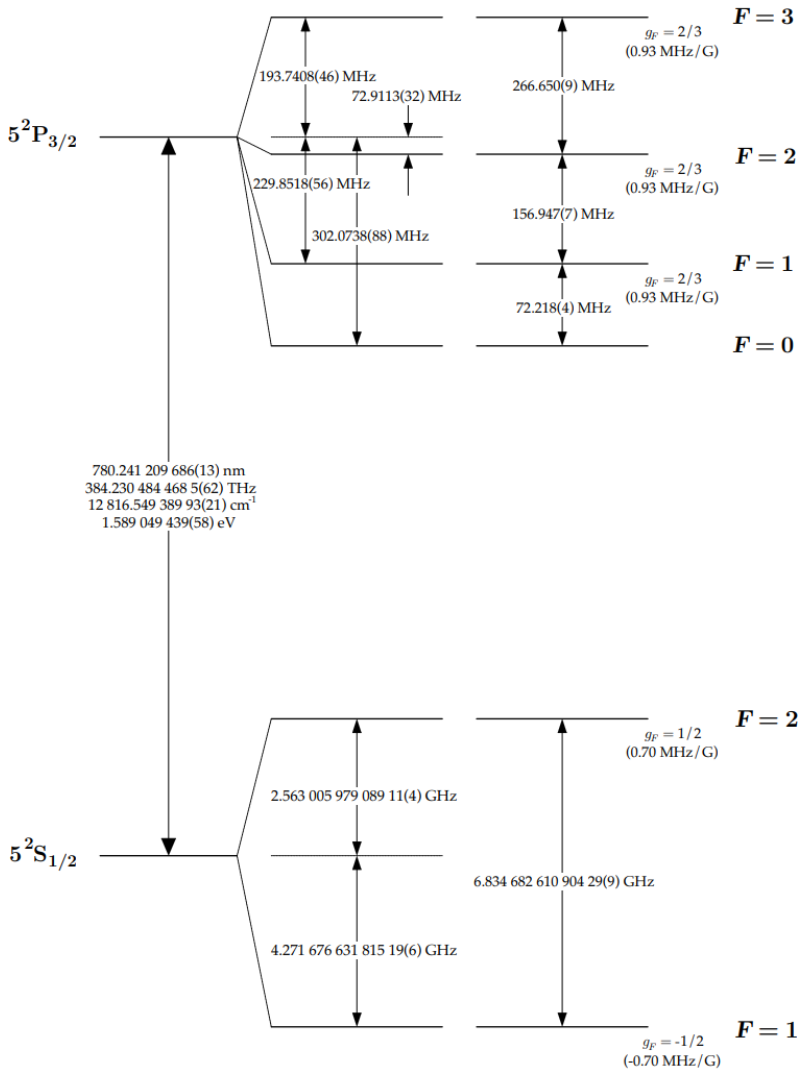

Figure 2.1: Rb-87 D2 line hyperfine structure. (The frequency expression in this figure is frequency instead of angular frequency.) [4]

structure is displayed in Figure 2.1. In this case, the F=2 to F'=3 optical transition is an ideal clock transition for various operations, such as imaging the atoms, which will be discussed in later sections.

Zeeman splitting on the hyperfine levels are due to the interaction between a weak magnetic field on an axis and the electron magnetic dipole moment; the general forms

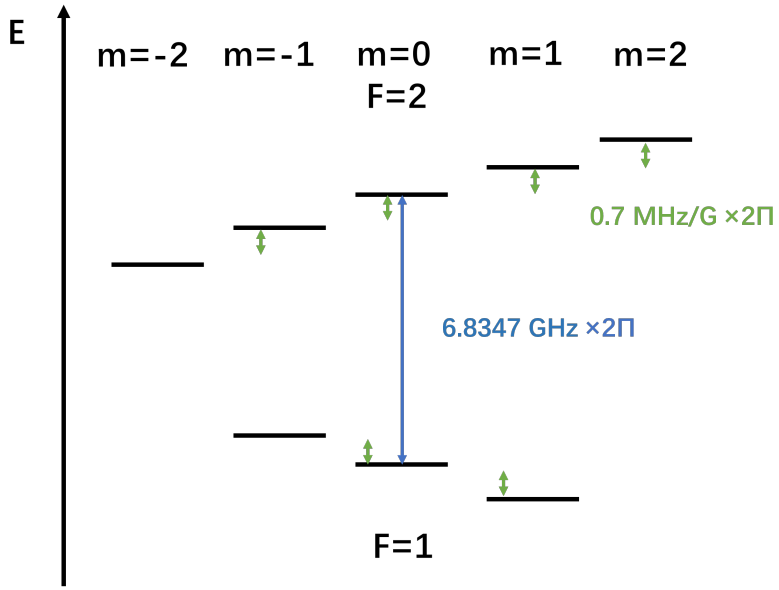

Figure 2.2: Zeeman Splitting on Rb-87 hyperfine levels

of the first and second orders of shift are defined by perturbation theory:

$$\Delta E^{(1)}_{F,m_F} = \left\langle F, m_F^{(0)} \middle| H_Z \middle| F, m_F^{(0)} \right\rangle = g_F \mu_B m_F B \tag{2.1}$$

The first-order Zeeman shift is linearly proportional to the quantum number m_F of the quantization axis. The Zeeman splitting of Rb-87 ground level is displayed in Figure 2.2.

2.2 Rabi Oscillation

Starting with semi-classical two-level atoms. Since we aim to perform an experiment in the Rb-87 ground level, the E1 interaction is forbidden because the electron doesn't change the orbit and the parity stays the same, so the M1 interaction dominates in this case. The Hamiltonian of the system can be expressed in (μ is the magnetic moment):

$$H_{\text{int}}(t) = -\boldsymbol{\mu} \cdot \mathbf{B}(t), \qquad \mathbf{B}(t) = \mathbf{B}_0 \cos(\omega t). \tag{2.2}$$

So

$$\hat{H}_{\text{int}} = -(\boldsymbol{\mu} \cdot \mathbf{B}_0)\cos(\omega t). \tag{2.3}$$

Write in the matrix format in basis of $\{|g\rangle, |e\rangle\}$:

$$\hat{H}_{\text{int}}(t) = \cos(\omega t)\begin{pmatrix} \langle g| - (\boldsymbol{\mu} \cdot \mathbf{B}_0)|g\rangle & \langle g| - (\boldsymbol{\mu} \cdot \mathbf{B}_0)|e\rangle \\ \langle e| - (\boldsymbol{\mu} \cdot \mathbf{B}_0)|g\rangle & \langle e| - (\boldsymbol{\mu} \cdot \mathbf{B}_0)|e\rangle \end{pmatrix}. \tag{2.4}$$

The two diagonal entries in the Hamiltonian representing the energy of two levels are nonzero, but will be time-averaged to 0. For the standard deviation, we keep only the transition-driving off-diagonal terms, giving the standard form similar to the E1 interaction:

$$\hat{H}_{\text{int}}(t) = \hbar\begin{pmatrix} 0 & \Omega \\ \Omega^* & 0 \end{pmatrix}\cos(\omega t), \tag{2.5}$$

where $\Omega = \frac{\langle g|H_{\text{int}}|e\rangle}{\hbar}$ is the Rabi frequency. Then, the total Hamiltonian will be:

$$\hat{H} = \hbar\begin{pmatrix} \omega_g & 0 \\ 0 & \omega_e \end{pmatrix} + \hbar\begin{pmatrix} 0 & \Omega \\ \Omega^* & 0 \end{pmatrix}\cos(\omega t), \tag{2.6}$$

where ω_g and ω_e are the bare ground state and excited state energy.

By substituting in the Schrodinger equation and applying the Rotating Wave Approximation, which eliminates the fast oscillating terms, the probability that atoms are in the excited and ground states will be:

$$P_e(t) = |c_e(t)|^2 = \left|\frac{\Omega}{\Omega'}\right|^2 \sin^2\left(\frac{\Omega' t}{2}\right), P_g(t) = 1 - P_e(t), \tag{2.7}$$

where the generalized Rabi frequency is $\Omega' = \sqrt{|\Omega|^2 + \delta^2}$, and $\delta = \omega_{eg} - \omega_{driving}$ is how much the driving microwave frequency is detuned from the aimed transition frequency.

If we assume that the detuning is small, then the state of the atom will oscillate between the ground state and the excited state, as shown in Figure 2.3.

In the demonstration of Rabi flopping on the Bloch sphere (Figure 2.4), we still apply a small detuning to the microwave and the current state vector $\vec{R}$ will follow

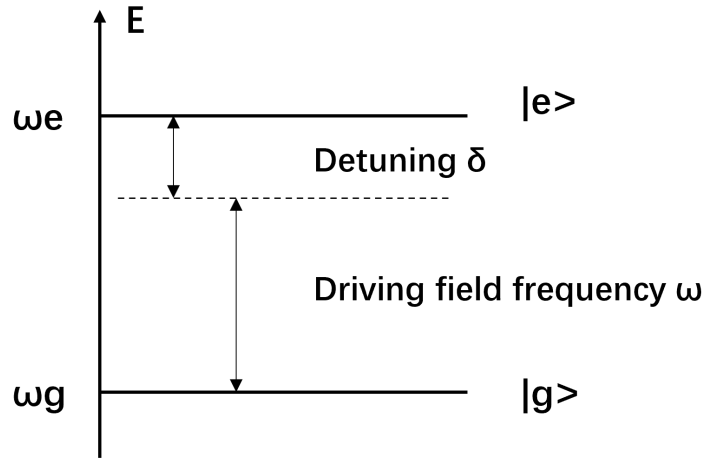

(a)

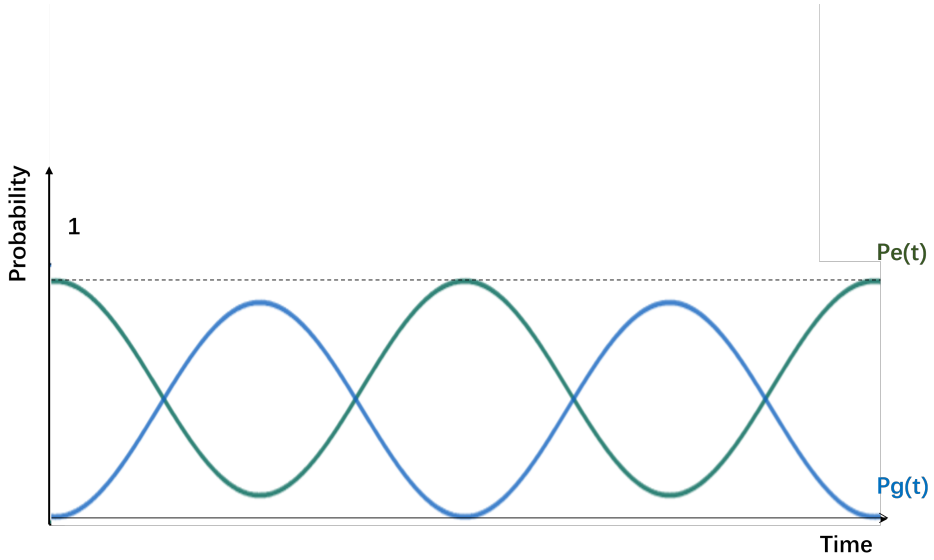

(b)

Figure 2.3: Figure (a) displays a two-level atom, which is coupled by a driving field with some detunings from the resonance frequency; Figure (b) illustrates the Rabi Oscillation between the ground state and the excited state in a two-level atom when the driving field has a very small detuning

$\frac{d\vec{R}}{dt} = \vec{\Omega} \times \vec{R}$ to rotate on the surface of the sphere, oscillating between the two states.

The latter 2.7 and 2.8 sections will revisit the Bloch sphere with more rigorous maths.

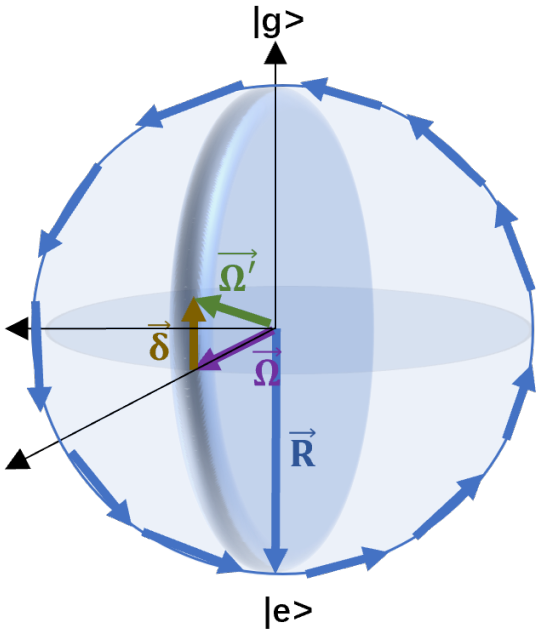

Figure 2.4: This figure illustrates the Rabi Oscillation on the Bloch sphere for a very small detuning δ on the driving microwave field.

2.3 AC Stark Shift

When applying a laser field to a two-level atom, the dressed atom Hamiltonian in the basis of $\{|g\rangle, |e\rangle\}$ is:

$$\hat{H} = \hat{H}_{\text{atoms}} + \hat{H}_{\text{field}} + \hat{H}_{\text{int}} = \begin{pmatrix} E_g & 0 \\ 0 & E_e \end{pmatrix} + \hbar\omega_{\text{l}} \begin{pmatrix} N+1 & 0 \\ 0 & N \end{pmatrix} + \hbar \begin{pmatrix} 0 & \Omega/2 \\ \Omega^*/2 & 0 \end{pmatrix} \tag{2.8}$$

$$\hat{H} = \hbar \begin{pmatrix} \Delta & \Omega/2 \\ \Omega^*/2 & 0 \end{pmatrix}$$

where $\Delta = \omega_l - \omega_{eg}$ is the laser frequency detuning value and Ω is the Rabi frequency between the two levels, so the eigen-energies are:

$$E_{e,g} = \hbar \frac{\Delta \pm \sqrt{\Delta^2 + |\Omega|^2}}{2} \tag{2.9}$$

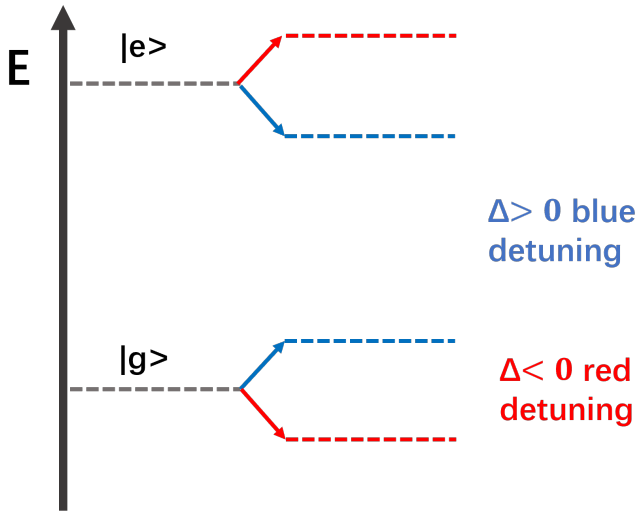

Figure 2.5: This figure illustrates the AC Stark shifts of the excited- and ground-state energy levels for different detuning values from the atomic resonance frequency.

Here, we only consider $|\Delta| \gg \Omega$ and apply Taylor expansion to simplifier the expression

$$\sqrt{\Delta^2 + |\Omega|^2} \approx |\Delta| + \frac{|\Omega|^2}{2|\Delta|}$$

Finally, we can get

$$E_g \approx \hbar\left(\frac{\Delta + |\Delta|}{2}\right) + \frac{\hbar|\Omega|^2}{4\Delta}, \qquad E_e \approx \hbar\left(\frac{\Delta - |\Delta|}{2}\right) - \frac{\hbar|\Omega|^2}{4\Delta} \quad , \tag{2.10}$$

where $\hbar\left(\frac{\Delta+|\Delta|}{2}\right)$ and $\hbar\left(\frac{\Delta-|\Delta|}{2}\right)$ are pure field energy and are not included in the interaction with the atom. According to formula 2.9, the excited state energy level shifts up $\frac{\hbar|\Omega|^2}{4|\Delta|}$ and ground state energy level shifts down $\frac{\hbar|\Omega|^2}{4|\Delta|}$ in red detuning and in the opposite way in blue detuning, which are shown in Figure 2.5.

2.4 Scattering Rate

In a quantum system, the state with higher energy can randomly decay to the state with lower energy by emitting a photon, and the process is called spontaneous emission. Assume we are dealing with a two-level atom with an optical transition.

The coherent two states in the quantum system will ultimately decay into a statistical mixture of states, so we can define the scattering rate as the decoherence rate in the quantum system, which will be discussed further in later sections.

The scattering rate of Rb-87 can be expressed as:

$$\gamma_{\text{scatt}} = \frac{\gamma}{2} \frac{s_0}{1 + s_0 + \left(\frac{2\Delta}{\gamma}\right)^2} \tag{2.11}$$

where γ is the natural decay rate of the atom, s_0 is the saturated intensity, which equals to $I/I_{\text{sat}} = 2\,|\Omega|^2/\gamma^2$ ($I_{\text{sat}} = \frac{\pi hc}{3\,\lambda^2\tau}$), and Δ is the detuning from atomic resonance frequency. Experimentally, we use various techniques, i.e., laser cooling and evaporation cooling, to cool Rb-87 atoms down to μK scale temperatures to largely suppress the linewidth broadening caused by the Doppler effect. Therefore, solely based on the formula, the scattering rate has a Lorentz distribution as a function of the detuning Δ, which means it is maximized at the resonance frequency and decays as it is further away from the resonance frequency. In the case of the 780 nm cycling transition in Rb-87, we have γ=$2\pi \times 6$ MHz and I_{sat}= 1.6 $\frac{mW}{cm^2}$

2.5 Scenarios for Imaging External Field with Rb-87 in MOT chamber

2.5.1 Imaging a laser beam

The basic scheme for imaging a laser beam is shown in Figure 2.6. The idea is to trap and cool the Rb-87 atoms using a magneto-optical trap, then load them into a magnetic trap and use optical pumping to transfer the unwanted states to the untrapped states to purify the F=2, m_F=2 state, and finally let the atoms free-fall for imaging. Next, we direct a $2\pi\times$ 6.8 GHz microwave magnetic field at the atoms using a waveguide to couple the two atomic ground levels, F=2 and F=1. If we let a far-detuned 780 nm laser pass through the atom cloud, we should theoretically

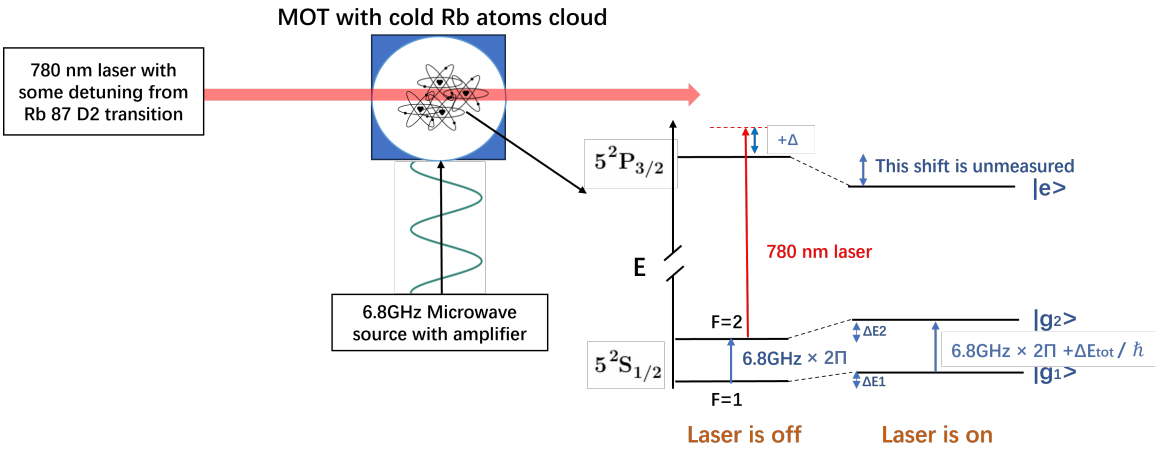

Figure 2.6: This figure displays the scenario for imaging a laser beam using cold Rb-87 atoms in the MOT chamber

generate the AC Stark shifts for both the F=1 and F=2 levels. In section 2.3, the thesis showed that using a laser field that is far detuned from the atomic resonance can minimize decoherence associated with the scattering rate. However, based on the calculation of energy-level shifts in section 2.2, the shift will become increasingly small as the detuning increases. As a result, we performed numerical simulations to find an acceptable balance between minimizing decoherence and maximizing the differential energy shifts, as shown in Figure 2.7.

Note that in the experiment, the laser can create $5P_{\frac{3}{2}}$ optical transitions from either of the F=1 or F=2 on ground levels to first excited state, and the energy level shifts of the two levels may be in the same direction or different directions and magnitude, so we want to measure the differential energy level shifts of two ground levels. Therefore, we use F=2 as a reference level for zero frequency detuning, and the Figure 2.7 subgraphs (a), (b), (c) correspond to the relationship plots for total energy level shifts and scattering rate under different detuning ranges.

According to equation 2.11 and Figure 2.6, the scattering rate equation for F=1

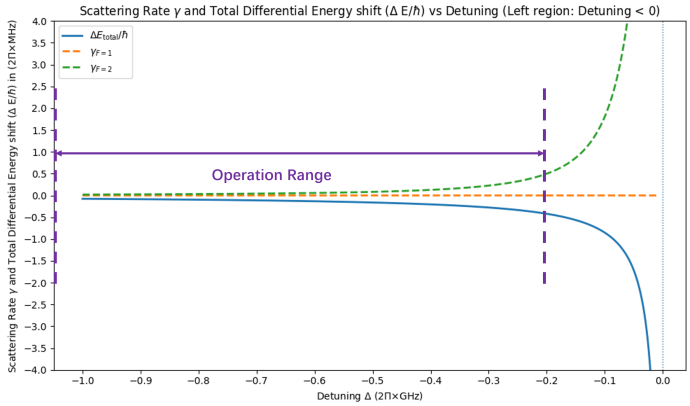

(a)

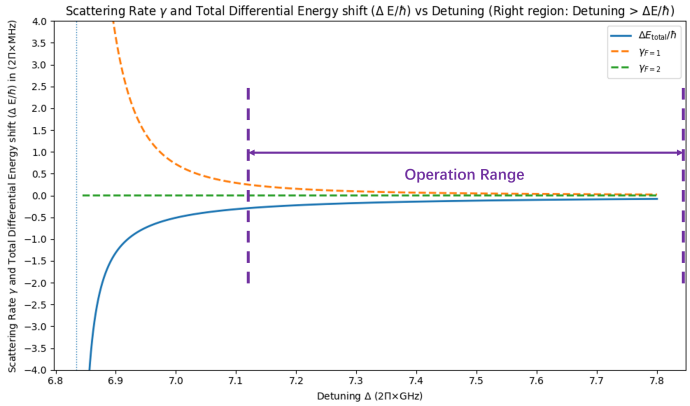

(b)

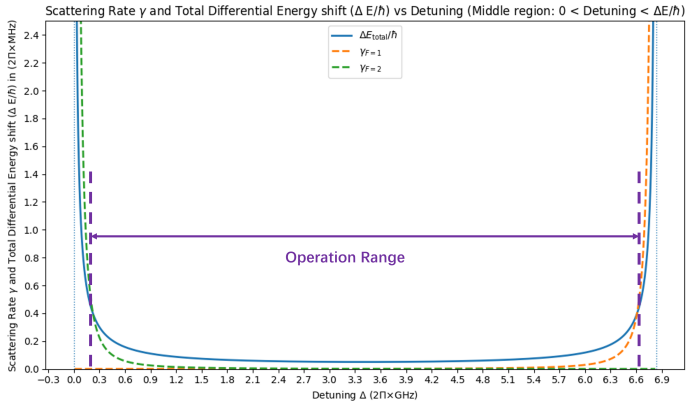

(c)

Figure 2.7: These three diagrams illustrate the relationships among scattering rate, energy-level shifts, and laser-frequency detuning.

and F=2 should be represented as ($\Delta E/\hbar = \Delta\omega_{12} \approx 2\pi \times 6.835\ GHz$):

$$\gamma_{\mathrm{F}=1} = \frac{\gamma}{2}\frac{s_0}{1+s_0+\left(\frac{2(-\Delta\omega_{12}+\Delta)}{\gamma}\right)^2}, \gamma_{\mathrm{F}=2} = \frac{\gamma}{2}\frac{s_0}{1+s_0+\left(\frac{2\Delta}{\gamma}\right)^2} \tag{2.12}$$

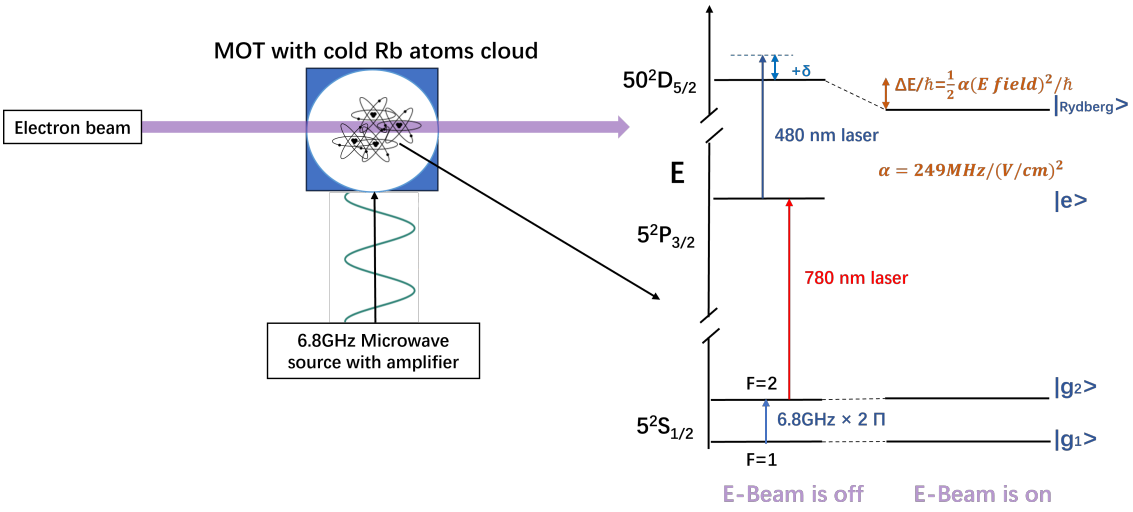

Figure 2.8: This figure displays the scenario for imaging an electron beam using cold Rb-87 atoms in the MOT chamber

Additionally, the AC stark shift of two levels based on equation 2.10 should be represented as (in the far detuned limit):

$$\Delta E_{F=1} = \frac{\hbar\,|\Omega|^2}{4(-\Delta\omega_{12}+\Delta)}, \Delta E_{F=2} = \frac{\hbar\,|\Omega|^2}{4\Delta}, \Delta E_{total} = \frac{\hbar\,|\Omega|^2}{4(-\Delta\omega_{12}+\Delta)} + \frac{\hbar\,|\Omega|^2}{4\Delta}, \tag{2.13}$$

Based on the simulation results (see Figure 2.7), there will be three ideal operating laser frequency regions, where the magnitudes of both the scattering rate and the total energy-level shift are within an appropriate range. And the laser frequency needs to be detuned at least around $2\pi\times$ 0.3 GHz.

2.5.2 Imaging an electron beam

Though my work focuses on imaging a laser beam, in this subsection, I will show the basic concept for imaging an electron beam. As shown in Figure 2.8, we intend to use two lasers to excite the Rb-87 atom from the ground state to the Rydberg state, which is more sensitive to electric fields and long-lived enough to perform the experiment. When the electron beam interacts with Rb-87, the Rydberg state will

experience the energy level shift; the ground level shifts are negligible, and the shift will be proportional to the electric field squared of the electron beam. The DC stark shift for a Rydberg level is given by $\Delta E_{stark} = -\frac{1}{2}\alpha \left|E_{DC}\right|^2$. In the case of n=50, $D_{\frac{5}{2}}$ level, α=249 $\frac{MHz}{(\frac{V}{cm})^2}$ For comparison, $5S_{\frac{1}{2}}$ level, we have α=0.0794 $\frac{Hz}{(\frac{V}{cm})^2}$ [5] [6].

2.6 Adiabatic Rapid Passage

Adiabatic Rapid Passage (ARP) is a robust way to transfer state population between two levels by sweeping the frequency of an external field through resonance while keeping a non-zero coupling. In Figure 2.9, the two diagonal orange straight lines represent the two unperturbed states in the two-level atom. In our experiment, we use a microwave field to couple the two levels, and the dressed states, shown as the green curves, exhibit an avoided crossing, with the two ends of the curve extending along the directions of the unperturbed states.

If we set a frequency sweep starting point far away from the resonance frequency and choose a proper sweep range, we can transfer the atom state from one to another by performing the microwave frequency sweep. The frequency sweep rate should be slower than the Rabi frequency to avoid the Landau-Zener transition and faster than the decoherence rate between the two states.

2.7 Ramsey Interferometry

Section 2.2 showed that we intend to couple the two ground levels in Rb-87 via the microwave M1 transition, and the driving microwave frequency will result in the Rabi flopping between the two states of an atom.

According to equation 2.1, we choose to perform Ramsey Interferometry between $|2,0>$ and $|1,0>$ because these two states are not magnetically sensitive. Starting from the pure $|2,0>$ state, we can create a 50/50 superposition of $|1,0>$ and $|2,0>$

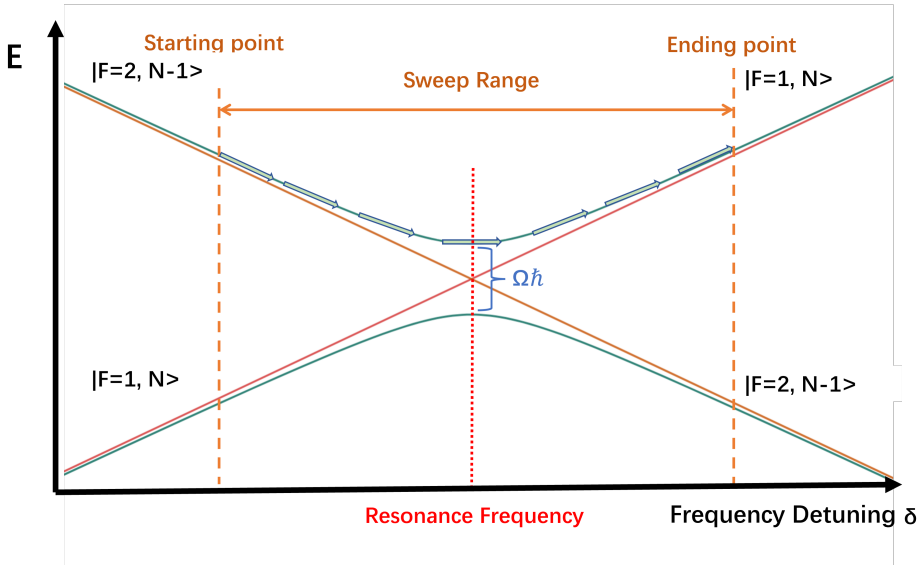

Figure 2.9: This figure illustrates Adiabatic Rapid Passage based on dressed states of a two-level atom. N represents the number of microwave photons. The orange diagonal straight lines represent the two unperturbed states: the ground state and the excited state. The two light-green curves represent the dressed states under the microwave coupling.

states by turning off the microwave on the equator of the Bloch sphere, which is also called a $\pi/2$ pulse and displayed in Figure 2.10(a). According to equation 2.7, we can compute the $\pi/2$ pulse time by $P_{|1,0>}(t) = \left|\frac{\Omega}{\Omega'}\right|^2 \sin^2\left(\frac{\Omega' t}{2}\right) = \frac{1}{2}$, such that the $\pi/2$ pulse time $T_{\pi/2} = \frac{2}{\Omega'} \sin^{-1}\left(\frac{\Omega'}{\sqrt{2}\,\Omega}\right)$.

Equation 2.8 can be expressed in Pauli matrix format (in the same basis):

$$\hat{H} = \hbar \begin{pmatrix} \delta/2 & \Omega/2 \\ \Omega^*/2 & -\delta/2 \end{pmatrix} = \frac{\hbar}{2} \left(\delta \hat{\sigma}_z + \Omega \hat{\sigma}_x\right), \tag{2.14}$$

And then the Rabi frequency vector $\vec{\Omega} = (\delta, 0, \Omega)$ and the Pauli matrix vector $\hat{\vec{\sigma}} = (\hat{\sigma}_z, \hat{\sigma}_y, \hat{\sigma}_x)$ defines the Cartesian coordinate of the Bloch Sphere. We can define the unit Rabi frequency vector $\vec{n} = (\frac{\delta}{\Omega'}, 0, \frac{\Omega}{\Omega'})$ and express $\hat{H} = \hbar \frac{\Omega'}{2} (\vec{n} \cdot \hat{\vec{\sigma}})$.

For a typical time-evolution operator, $\hat{U}(t) = e^{-i\hat{H}t/\hbar}$, The exponential has the property:

$$e^{-i(\vec{n}\cdot\vec{\sigma})a/2} = \hat{I} \cos\frac{a}{2} - i(\vec{n} \cdot \hat{\vec{\sigma}}) \sin\frac{a}{2} \tag{2.15}$$

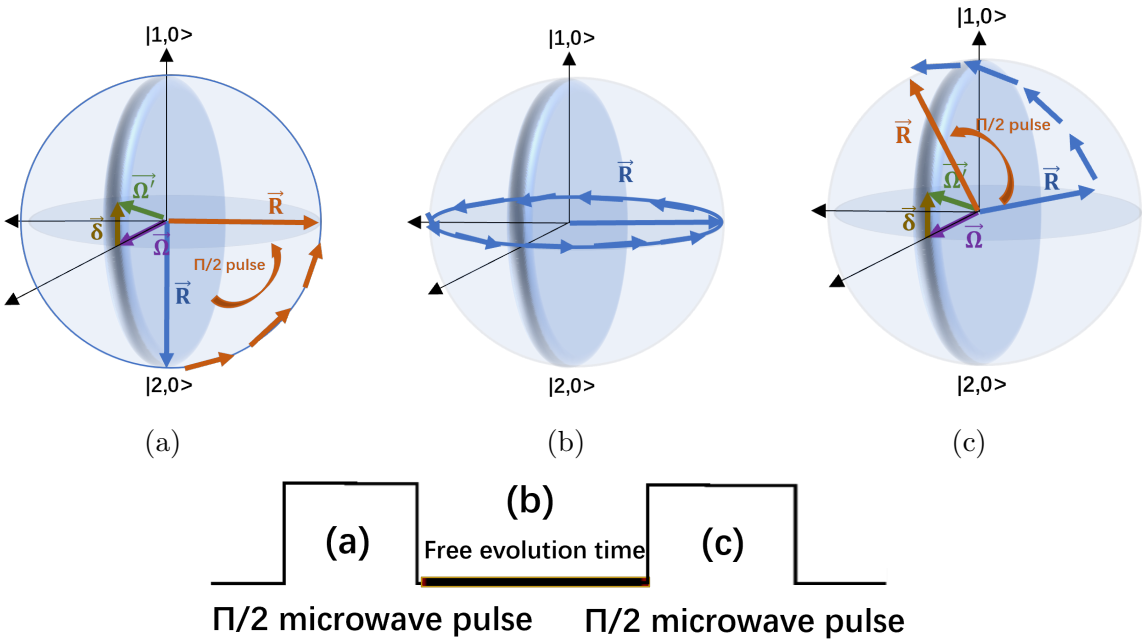

Figure 2.10: These four pictures demonstrate the atomic state during Ramsey Interferometry on the Bloch Sphere: (a) First $\pi/2$ pulse, (b) Free evolution, (c) Second $\pi/2$ pulse, (d) Ramsey interferometry time sequence. The z-axis represents the probability that the current state, R, projects on the $|1,0>$ or $|2,0>$ state. The x-y plane displays the phase of the current state.

Therefore,

$$\hat{U}(T_{\pi/2}) = \hat{I}\cos\frac{\Omega' T_{\pi/2}}{2} - i\left(\frac{\Omega}{\Omega'}\hat{\sigma}_x - \frac{\delta}{\Omega'}\hat{\sigma}_z\right)\sin\frac{\Omega' T_{\pi/2}}{2}. \tag{2.16}$$

Experimentally, we use a small detuning value, so the 50/50 superposition state vector nearly rotates along the x-axis, from the positive z-axis to the negative y-axis under this $\pi/2$ pulse, which follows the same rotation motion $\frac{d\vec{R}}{dt} = \vec{\Omega} \times \vec{R}$ mentioned in the earlier Rabi flopping section (section 2.2).

Ramsey Interferometry basically detects the detuning or rather detuning $\times$ time of the driving field from the atomic resonance as the state population ratio oscillates under the phase accumulation. Figure 2.10(b) shows that the atomic states are under phase accumulation, rotating on the equator. During the free evolution, there is no

driving field, and equation 2.8 can be written as:

$$\hat{H} = \hbar \begin{pmatrix} \delta/2 & 0 \\ 0 & -\delta/2 \end{pmatrix} = \frac{\hbar}{2} (\delta \hat{\sigma}_z) . \tag{2.17}$$

The operator during this period can be expressed as (τ is the free evolution time):

$$\hat{O}(\tau) = \hat{I} \cos\left(\frac{\delta\tau}{2}\right) + i \sin\left(\frac{\delta\tau}{2}\right) \hat{\sigma}_z = \begin{pmatrix} e^{i\delta\tau/2} & 0 \\ 0 & e^{-i\delta\tau/2} \end{pmatrix} \tag{2.18}$$

According to Equation 2.14, the state will rotate around the z-axis. The direction and speed of evolution will depend on the sign and magnitude of the detuning between the driving microwave field and the two levels' resonance frequencies. Section 2.3 has shown that a laser beam can cause a differential AC Stark shift between the two coupled states. The change in atomic resonance frequency means the actual detuning of the driving field will also change. The differential shifts of energy will transform into the phase information of the state.

The second $\pi/2$ pulse is necessary to read out the state population ratio, which is shown in Figure 2.10(c). The operator expression is the same as equation 2.14. The total Ramsey time sequence is illustrated in Figure 2.10(d). The total operator then becomes $\hat{T}(\tau) = \hat{U}(T_{\pi/2})\hat{O}(\tau)\hat{U}(T_{\pi/2})$. For the final probability readout of atoms in the $|1,0>$ state, $P_{|1,0>} = \left|\langle 1,0|\hat{T}(\tau)|2,0\rangle\right|^2 = \left|(\hat{T}(\tau))_{12}\right|^2$. By calculation,

$$\begin{aligned} (\hat{T}(\tau))_{12} &= -i\frac{\Omega}{\Omega'}\left[\sin(\Omega' T_{\pi/2}) \cos\left(\frac{\delta\tau}{2}\right) - 2\frac{\delta}{\Omega'} \sin^2\left(\frac{\Omega' T_{\pi/2}}{2}\right) \sin\left(\frac{\delta\tau}{2}\right)\right] \\ &= -i\left[\sqrt{1 - \frac{\delta^2}{\Omega^2}} \cos\left(\frac{\delta\tau}{2}\right) - \frac{\delta}{\Omega} \sin\left(\frac{\delta\tau}{2}\right)\right]. \end{aligned} \tag{2.19}$$

If we assume that $\delta << \Omega$, the probability expression becomes:

$$P_{|1,0>} = \cos^2\left(\frac{\delta\tau}{2}\right) \tag{2.20}$$

If δ is not negligible comparing to Ω, we can define $sin(\Phi) = \frac{\delta}{\Omega}$. Then the probability expression will be:

$$P_{|1,0>} = \cos^2\left(\frac{\delta\tau}{2} + \Phi\right) \tag{2.21}$$

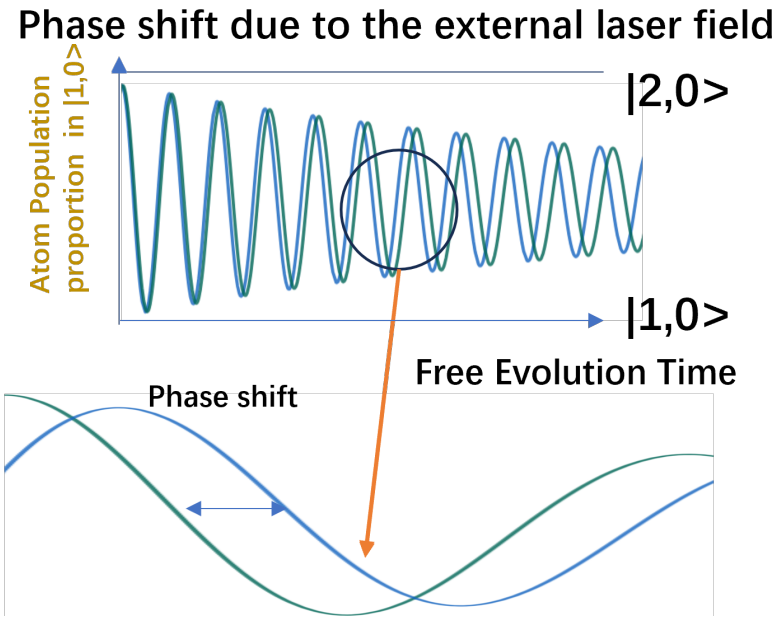

Figure 2.11: Stimulated Ramsey fringes and shifts due to the laser field

Next, we assume that an external laser field is applied to the atom cloud during the free evolution period, causing AC Stark shifts on $|1,0>$ or $|2,0>$. If the total differential energy shift between two levels is nonzero, the detuning between the driving microwave and the resonance frequency of $|1,0>$ or $|2,0>$ will change. Here, we define the new detuning value as δ'. Then the probability expression will be:

$$P_{|1,0>} = \cos^2\left(\frac{\delta'\tau}{2} + \Phi\right) \tag{2.22}$$

Compared to equation 2.21, the Ramsey fringe oscillation rate will change. On a relatively long timescale, the two fringes will exhibit a clear phase difference, as shown in Figure 2.11.

During free evolution, the scattering rate determines the number of photons emitted by atoms into the environment. Then the emitted photons, which carry the atoms' information, will interact with the environment. During the interactions, the atom phase information will gradually be lost, in simpler words, decoherence. In the

real experiment, the scattering rate will remain constant because the laser power will remain constant. Over longer evolution times, more photons will be emitted, leading to more interactions and a decay of the Ramsey fringe signal due to decoherence.

If we select the middle region in Figure 2.7 (c), we expect the total differential energy shift (in angular frequency) to be around $2\pi\times$ (+)0.1 MHz. One trick we can use to avoid the fringes oscillating too fast is to set the detuning of the microwave driving field to be in the opposite sign of the AC Stark energy shift.

2.8 Spin Echo

The latter chapter will raise concerns about the unknown magnetic gradient around the experimental apparatus. This section mainly discusses the Spin Echo technique, which is similar to Ramsey Interferometry but provides greater resistance to phase changes induced by environmental noise (e.g., magnetic field gradients).

As mentioned in Section 2.1, the first-order Zeeman shift is linearly proportional to the quantum number m_F of the quantization axis.

$$\Delta E^{(2)}_{F,m_F} = \sum_{F' \neq F} \frac{|\langle F', m_F|H_Z|F, m_F\rangle|^2}{E^{(0)}_F - E^{(0)}_{F'}} \tag{2.23}$$

The second-order Zeeman shift is a result of a mixture of different hyperfine states with the same m_F quantum number. Based on equation 2.23, the second-order Zeeman shift is not directly proportional to m_F, so choosing the $|2, 0>$ to $|1, 0>$ transition can make the first-order Zeeman shift zero but still have the second-order effect.

Spin Echo has similar concepts to Ramsey Interferometry, but can minimize the effect of the second-order Zeeman shift during the free evolution time due to the unexpected magnetic gradient. The total operation sequence is shown in Figure 2.12. The population probability of $|1, 0>$ after a perfect π pulse is 1, and the detuning of the driving microwave field should be 0 during the pulse according to equation 2.17.

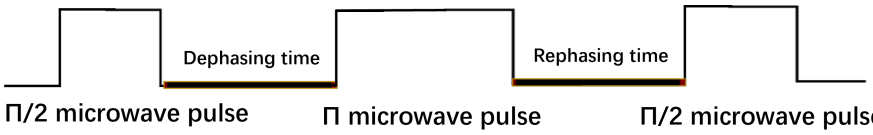

Figure 2.12: The first $\pi/2$ pulse creates a superposition between $|1,0>$ and $|2,0>$ and allows the first free evolution period to dephase the atom cloud. Then, applying a π pulse to reverse the direction in which spin states evolve to rephase the atom cloud. The second $\pi/2$ pulse is used to read out the population.

We can get the π pulse operator from equation 2.16:

$$\hat{M}(T_\pi) = I\cos\frac{\Omega' T_\pi}{2} - i\left(\frac{\Omega}{\Omega'}\sigma_x - \frac{\Delta}{\Omega'}\sigma_z\right)\sin\frac{\Omega' T_\pi}{2} = -i\sigma_x \tag{2.24}$$

The operator basically rotates the state 180 degrees about the x-axis on the Bloch sphere. If the magnetic gradient is stable for this amount of time, the states will then evolve in the opposite direction about the z-axis after the π pulse, compared to the first evolution period. This will cancel out most of the effects brought about by the static magnetic gradient.

The total operator then becomes $\hat{T}(\tau_1,\tau_2) = \hat{U}(T_{\pi/2})\hat{O}(\tau_2)\hat{M}(T_\pi)\hat{O}(\tau_1)\hat{U}(T_{\pi/2})$. By calculation,

$$\begin{aligned}(\hat{T}(\tau_1,\tau_2))_{12} &= -i\left[\left(\cos^2\frac{\Omega' T}{2} + \frac{\Delta^2}{\Omega'^2}\sin^2\frac{\Omega' T}{2}\right)e^{i\Delta(\tau_2-\tau_1)/2} - \frac{\Omega^2}{\Omega'^2}\sin^2\frac{\Omega' T}{2}e^{-i\Delta(\tau_2-\tau_1)/2}\right] \\ &= -i\left[\frac{1}{2}e^{i\Delta(\tau_2-\tau_1)/2} - \frac{1}{2}e^{-i\Delta(\tau_2-\tau_1)/2}\right] \\ &= -\sin\left(\frac{\Delta(\tau_2-\tau_1)}{2}\right)\end{aligned} \tag{2.25}$$

Therefore, $P_{|1,0>} = \left|\langle 1,0|\hat{T}(\tau_1,\tau_2)|2,0\rangle\right|^2 = \left|(\hat{T}(\tau_1,\tau_2))_{12}\right|^2 = \sin^2\left(\frac{\Delta(\tau_2-\tau_1)}{2}\right)$.

Practically, the trend of the whole signal fringes should still fade away because the scattering photons have a significant effect, and the echo will recover a little bit of coherence by rephasing the atoms, so the decoherence effect brought by the magnetic gradient will be minimized in this case. According to equation 2.25, the

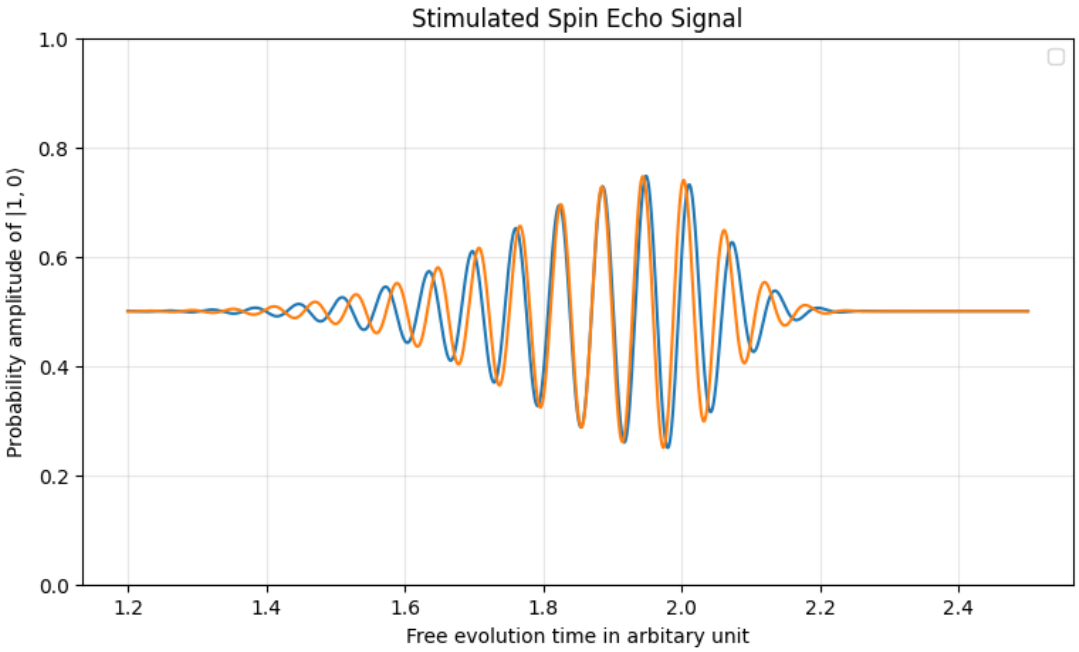

Figure 2.13: Stimulated Spin Echo fringes and shifts due to the laser field. The two fringes in different colors display the shifts due to the atom-laser field interaction during the first free evolution period

fringe oscillation frequency will change in response to the change of detuning during the free evolution period, and $P_{|1,0>} = \sin^2\left(\frac{\Delta_2\tau_2 - \Delta_1\tau_1}{2}\right)$. The stimulated Spin Echo signal is shown in Figure 2.13, where the blue signal corresponds to the same driving field detuning during the two evolution times, and the orange signal corresponds to the different driving field detuning Δ_2 and Δ_1 during the two evolution times due to the AC Stark shifts.

Chapter 3

Experimental Apparatus

This chapter gives a brief overview of the ultracold Rb-87 apparatus, and then proceeds to describe two significant additions to this apparatus that were necessary for this Ramsey imaging project: 1) the development of an agile microwave frequency source at $2\pi\times$ 6.8 GHz and 2) an imaging system and scheme for measuring state population ratios. Note that all frequencies in this chapter are expressed as angular frequency.

3.1 Brief Overview of Ultracold Atom Apparatus

Figure 3.1 depicts the main ultracold atom apparatus, which was made by Megan Ivory and Austin Ziltz. We use Rb87 atoms in the experiment, which are cooled by Doppler cooling and trapped in a magneto-optical trap (MOT) in a vacuum chamber. Next, the atoms are confined in a magnetic trap, where they are further cooled by evaporative cooling, and the state population is purified so that only $|F = 2,\ m_F = 2>$ ground state atoms are trapped. In the MOT region, we can apply evaporative cooling to further cool the atom cloud, so that the cloud expands slowly and has a smaller volume when the trap is turned off. The smaller volume experiences a smaller range of magnetic field values in a magnetic gradient region. Alternatively, if we want to proceed with the experiment on the atom chip region, a set of magnetic

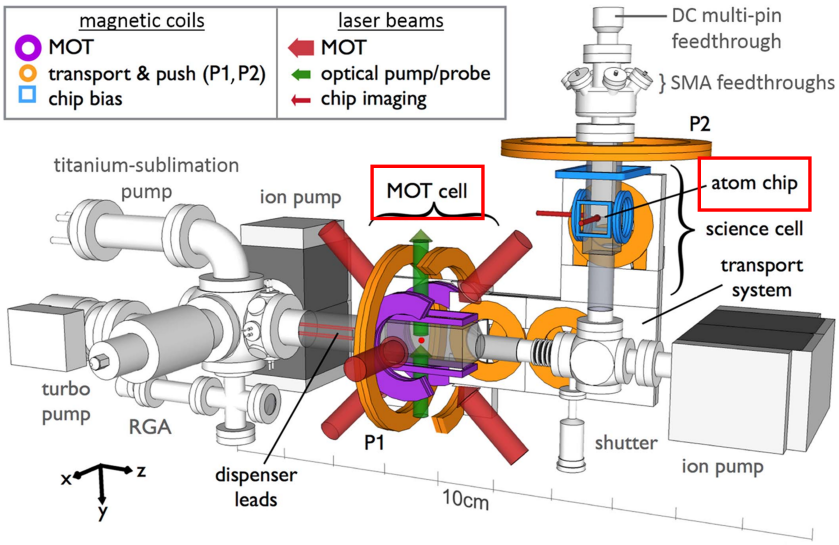

Figure 3.1: Main ultracold atom apparatus [7] [8]

coils will transfer the atoms to the atom chip trap. The atom chip region will be further discussed in Chapter 4.

3.2 Microwave System

We developed a phase-continuous, phase-stable, and low-noise microwave source capable of performing frequency sweeps. Importantly, I want to credit William Miyahira, who made the first such system in the lab. A basic block diagram of the system is shown in Figure 3.2. The overall goal of this microwave system is to output a signal with rapidly controllable frequency and phase around $2\pi\times$ 6.8 GHz for performing state manipulations, such as $\pi/2$ pulses and adiabatic rapid passage.

In order to generate a phase-continuous, agile, ultrastable $2\pi\times$ 6.8 GHz microwave source with ultralow phase noise, we begin with two frequency sources:

1) An ultrastable, $2\pi\times$ 3.2 GHz source with ultralow phase noise (Holzworth HSM4001B, see Fig 3.3 (b), which unfortunately is not sufficiently agile (i.e., it cannot conveniently do fast frequency sweeps))

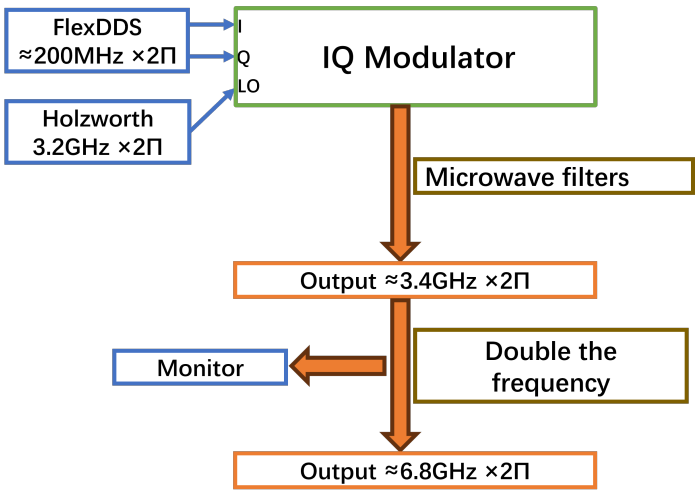

Figure 3.2: Logic diagram of our microwave system

2) A very stable, $2\pi\times$ 1-400 MHz source with very low phase noise (FlexDDS, see Fig 3.3(a)), which is also very agile (phase continuous, frequency and phase sweeps or adjustments).

These two sources are combined via IQ modulation (see Figure 3.3 (c)) to generate an agile, but very stable $2\pi\times$ 3.4 GHz source with ultralow phase noise. This 3.4 GHz signal is then doubled to $2\pi\times$ 6.8 GHz and then directed towards the atoms using a "sawed off" waveguide.

The FlexDDS, based on the AD9910 chip, outputs two RF signals around $2\pi\times$ 200 MHz with a 90-degree phase difference. The Holzworth, as the other raw frequency source, generates a constant $2\pi\times$ 3.2 GHz signal. These two frequency sources are also connected to an external Rb clock to synchronize their internal time ticks. They are displayed in Figure 3.3 (a) and (b).

Next, these three signals are combined by the IQ-Modulator shown in Figure 3.3(c) to produce a single signal around $2\pi\times$ 3.4 GHz after passing through several microwave filters. The basic operation logic diagram inside the IQ-Modulator is shown in Figure 3.4. The I and Q channels represent the two FlexDDS signals, and the LO

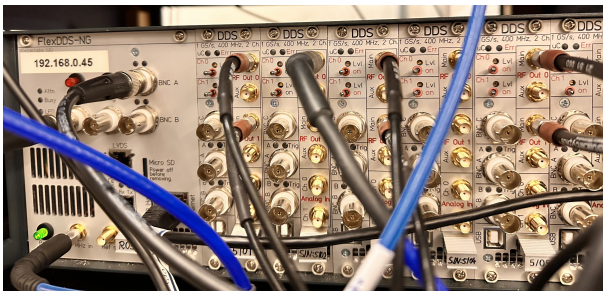

(a)

(b)

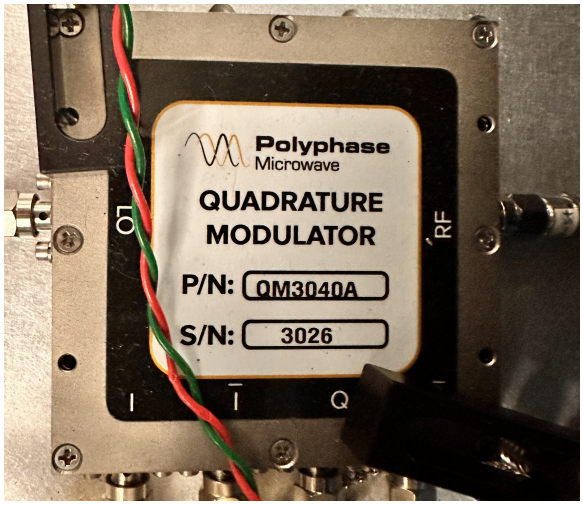

(c)

Figure 3.3: Microwave system components: (a) FlexDDS RF source ($2\pi\times$ 1-400 MHz), (b) Holzworth microwave source for ultralow phase noise at $2\pi\times$ 3.2 GHz, (c) IQ-Modulator for combining the FlexDDS RF signals around $2\pi\times$ 200 MHz and Holzworth microwave $2\pi\times$ 3.2 GHz signal to around $2\pi\times$ 3.4 GHz. It doesn't double $2\pi\times$ 3.4 GHz to $2\pi\times$ 6.8 GHz.

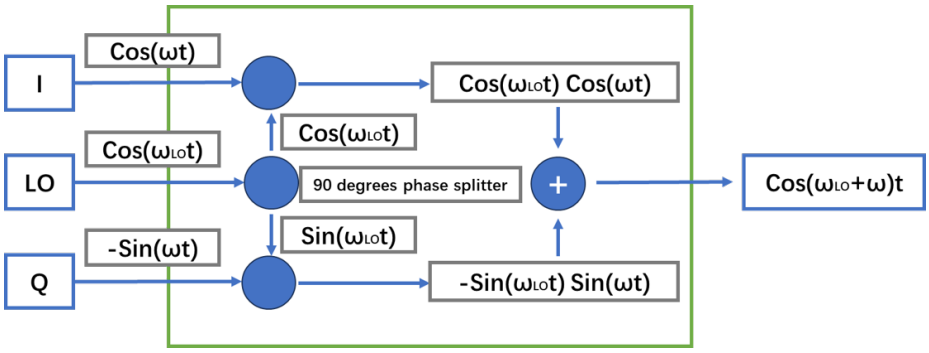

Figure 3.4: Logic diagram of the IQ-Modulator

channel represents the Holzworth signal. The signal in the LO channel will first be split by a 90-degree phase splitter, then the split signals will multiply the signals on either the I or Q channel, and the final operation block adds the two signals from the two arms. Therefore, if the I and Q channels have $2\pi\times$ 200 MHz input signals and the LO channel has a $2\pi\times$ 3.2 GHz input signal, the IQ-Modulator's output signal will be $2\pi\times$ 3.4 GHz.

The microwave filtering system consists of low-pass filters, band-pass filters, and homemade pipe-cap filters. Most filters are designed to filter harmonic frequencies, and pipe-cap filters are specifically designed to filter out the $2\pi\times$ 3.2 GHz signal generated by Holzworth, which is not the signal at $2\pi\times$ 3.4 GHz (Figure 3.5).

The rest of the microwave system consists of the microwave amplifier, which not only amplifies the microwave amplitude but also doubles the frequency, and the monitoring system. The $2\pi\times$ 6.8 GHz signal will eventually be sent to the atom cloud either via a microwave antenna at the atom region or via a waveguide in the MOT region.

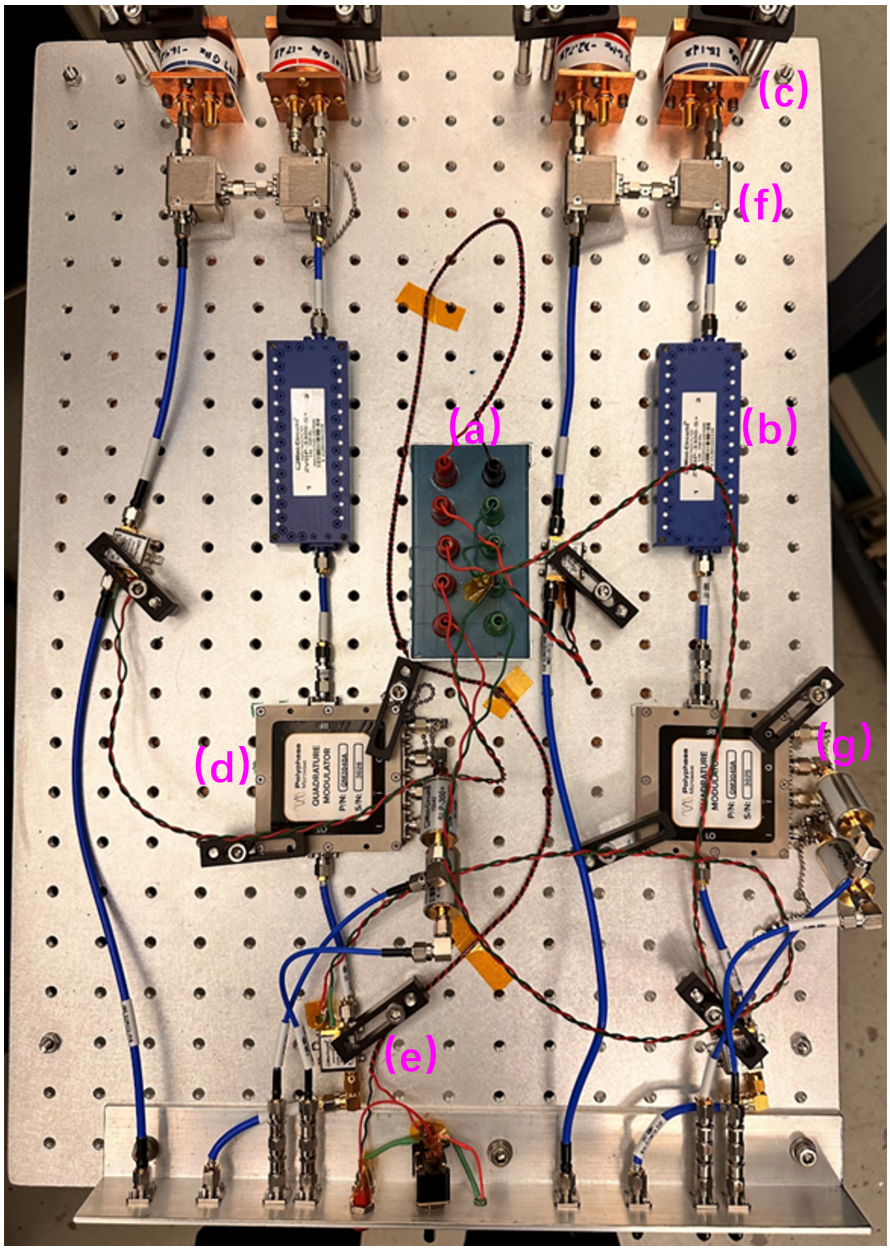

Figure 3.5: Full picture of IQ-Modulator based microwave system for generating around $2\pi\times$ 3.4 GHz microwave field: (a) A set of voltage regulators which convert around 7-12 V to a stable 5 V; (b) ZVBP-3300-S+ Mini-Circuits band pass filters ($2\pi\times$ 3100 - 3500 MHz); (c) Pipe-cap filters which are especially designed for filtering $2\pi\times$ 3.2 GHz signal; (d) IQ Modulator (descriptions are in Figure 3.3); (e) ZX60-83LN-S+ Mini-Circuits wide band microwave amplifiers; (f) Microwave circulators; (g) SLP-300+ low pass filter Mini-Circuits (DC to $2\pi\times$ 270 MHz).

3.3 Imaging System

We use two methods to image the atoms, absorption imaging and fluorescence imaging. For both imaging methods, we use laser beams derived from the same laser source, which is either a resonance or detuned by a few atomic linewidths. The basic concept of absorption imaging is that atoms absorb photons from the imaging probe laser, so that we can determine the atom cloud population by measuring the shadow they produce in the laser field. Fluorescence imaging provides a more direct measurement: since atoms jump to excited states after absorbing photons, they undergo spontaneous emission, emitting light in all directions. By measuring the photons emitted by the atoms, we can also know the atomic population.

CCDs are used to detect the atom population and spatial information with around 24 dB camera gain and the capability of performing at least 1-second exposures, but they only have around 30% quantum efficiency at wavelengths around 780 nm.

3.3.1 Imaging System on the Atom Chip

The imaging system in the Atom Chip region has been set to absorption imaging because atom populations are low but density is high, and absorption imaging can provide a more precise measurement. The overall setup is a 1:1 (image: object) double-lens imaging system with a CCD. The system can switch to fluorescence imaging by using the imaging beam on an orthogonal axis.

We are performing the experiment on Rb-87 ground states, and two laser beams, a repump laser and a probe laser, are used to excite atoms to do absorption or fluorescence imaging. The basic logic is shown in Figure 3.5. Both lasers are positively circular-polarized, which corresponds to $+\sigma$ optical transition. The repump laser excites the atoms on the F=1 state to the F'=1 state, and finally, all the atoms will decay to the F=2 state, and eventually, all the atoms are on the F=2 state. At

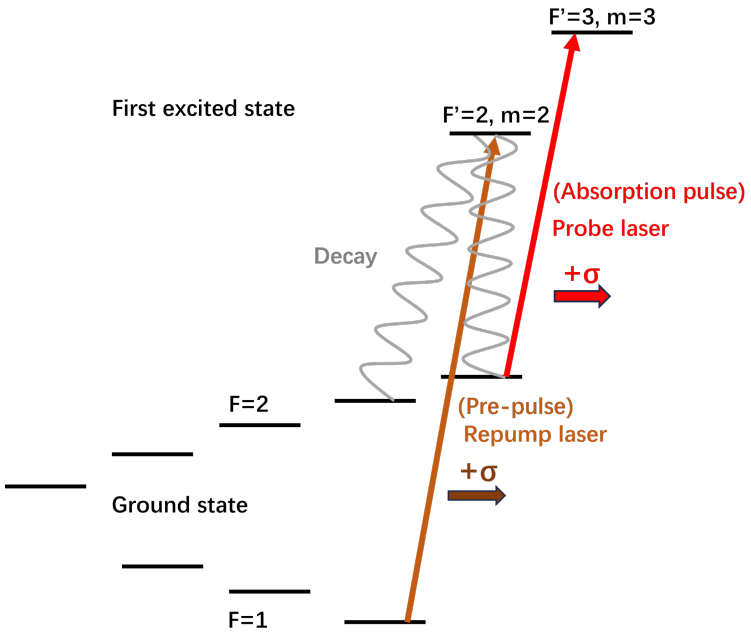

(a)

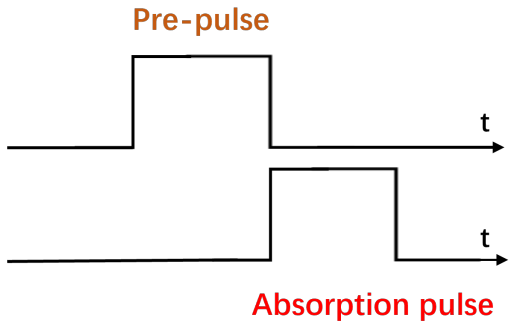

(b)

Figure 3.6: Laser pulse diagram for imaging atoms on the atom chip: (a) shows the laser transition for our probe laser and repump laser with hyperfine structure and Zeeman splitting; (b) displays the laser pulses in a time sequence. Each pulse lasts for around 2-5 ms.

the same time, the probe laser brings all the atoms to the F'=3 state, and because the F=2 to F'=3 transition is a cycling transition, we use it to image the total atom population. In the experiment, we prefer to measure the state population ratio between the population of one atomic state and the total atom population to mitigate the adverse effect of total atom population fluctuations shot-by-shot.

3.3.2 Imaging System in the MOT Region

In the MOT region, fluorescence imaging is used due to the high atom population, but lower atomic density, and the availability of higher laser intensity. We use FL3-FW-14S3 camera, which has 1384 $\times$ 1032 pixels, but we let it operate at 640 $\times$ 480 pixels in $2\pi\times$ 3.75 Hz mode. Pixel size is 4.65 μm $\times$ 4.65 μm.

The whole system is designed as an approximate 4.223:1 (object: image) single-lens imaging system and is mounted on the side of the MOT chamber to observe the spatial information of the atoms during free fall (Figure 3.6). A picture processed by the camera software displays the position and appearance of an atomic cloud in the MOT, as shown in Figure 3.7.

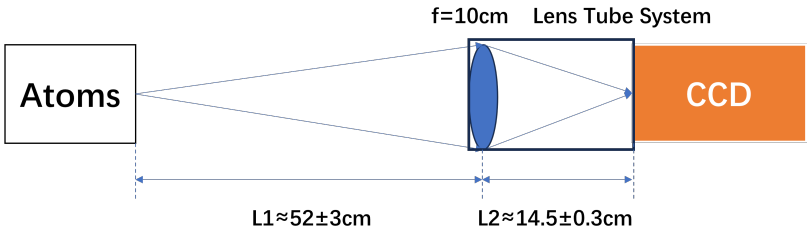

(a)

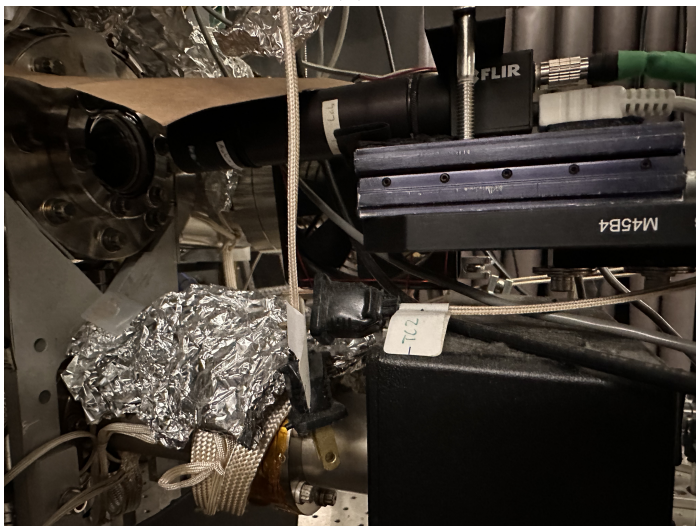

(b)

Figure 3.7: Imaging System Setup for MOT Region: (a) shows the diagram of each component in this imaging system and the distance relationship; (b) is a picture of the imaging system in real-time.

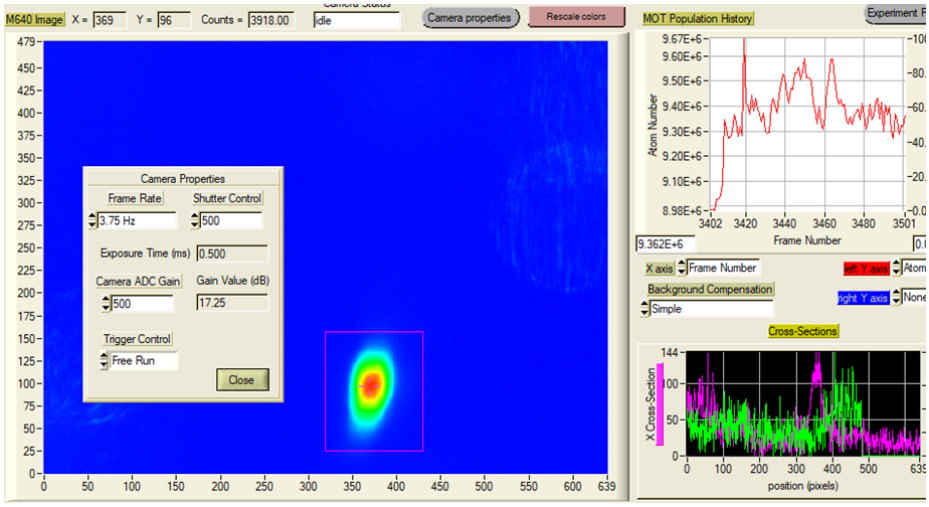

Figure 3.8: The Rb-87 atom cloud in the MOT

Chapter 4

Methodology and Results

This chapter mainly discusses the experimental results and the methodologies to achieve our research goal. Section 4.1 describes how we successfully performed the Ramsey Interferometry at the atom chip region. Section 4.2 describes the efforts we made to perform Ramsey Interferometry in the MOT region. Note that all frequencies in this chapter are expressed in angular frequency.

4.1 Ramsey Interferometry under Atom Chip

Since the apparatus (i.e., the coils for the Stern–Gerlach magnetic field gradient to separate atoms on different m_F states) is well provided at the chip region, we start to develop the techniques to perform Ramsey Interferometry between the $|F = 2, m_F = 0>$ and the $|F = 1, m_F = 0>$ states.

4.1.1 Atom Chip Trap

After atoms are cooled and trapped in the MOT chamber, they are delivered to the atom chip region by a magnetic trap-based transport system, and then transferred to the harmonic DC magnetic trap on the chip, which is shown in Figure 4.1.

We cool the atoms using evaporative cooling, but we do not cool them to the BEC, because we need to keep the atom population relatively high so we can still

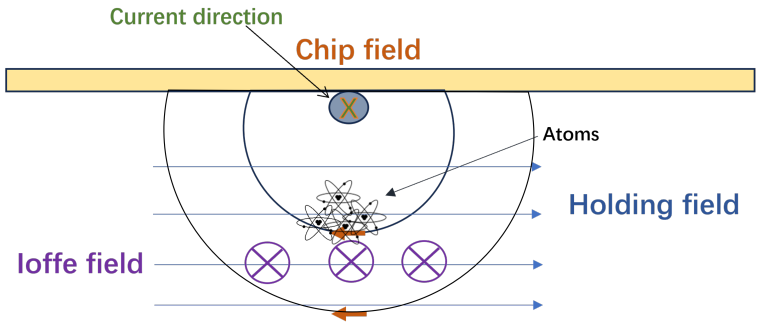

Figure 4.1: The DC magnetic trap on the atom chip only traps the low-field-seeker states. Here, the holding magnetic field, the chip magnetic field, and the Ioffe magnetic field combine to generate the harmonic trap potential. Ioffe magnetic field also makes the trap minimum not be zero to avoid the Majorana spin flipping.

get a good distribution signal from the atomic cloud after about 10 ms of free fall and thermal expansion. When turning off the magnetic trap and letting the atoms freely fall, we leave the Ioffe field on at a small value, typically a constant B_{Ioffe} = 5 G, to keep a relatively strong quantization field to avoid spin flips and create Zeeman splitting for further quantum manipulation of the atomic states. In theory, in a low magnetic field, 1 G can add an additional $2\pi\times$ 0.7 MHz of Zeeman splitting to any magnetically sensitive state. Hence, 5 G means the energy splitting between each Zeeman sublevel is $2\pi\times$ 3.5 MHz. The hyperfine levels and Zeeman sublevels of Rb-87 in the F=1 and F=2 ground states are shown in Figure 4.2.

4.1.2 Microwave operation

Generally, after turning off the chip trap, we wait about 3 ms before performing any microwave operation to avoid transient magnetic fields (e.g., from eddy currents). The initial states of the atoms after leaving the magnetic trap should be in the $|F = 2, m_F = 2 >$ state. We performed microwave spectroscopy on the specific $|2, 2 >$ to $|1, 1 >$ transition to determine the actual magnetic field in the experiment and the resonance frequency between these two states. The resonance scan in Figure

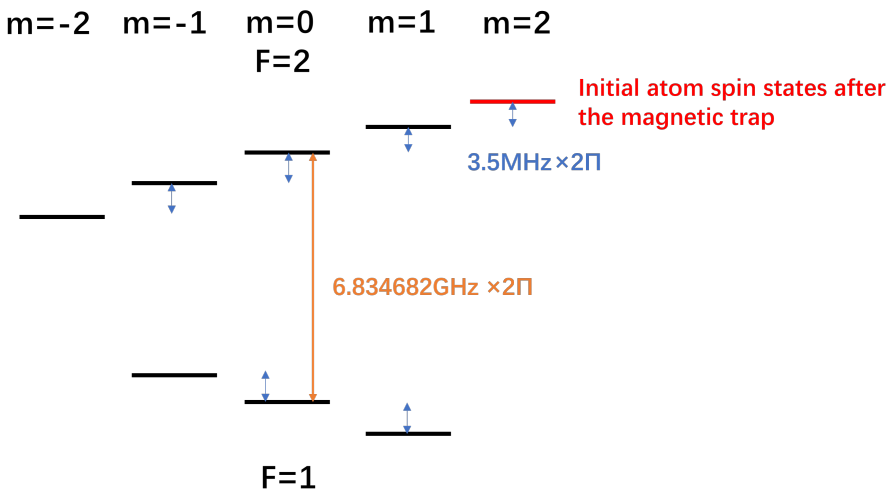

Figure 4.2: The hyperfine levels and Zeeman sublevels of Rb-87 under 5 G Zeeman splitting

4.3 shows that the resonance frequency is approximately $2\pi\times$ 6.84537 GHz, indicating that the environmental magnetic field is negligible in this case, and that the actual magnetic field is 5 G.

The microwave system has three basic controls: microwave amplitude, microwave mute, and TTL switch. Mute control operates more slowly than the TTL switch, but they both control the on-and-off of microwave power. In the experiment, we use the ADwin sequencer to generate the coarse microwave pulse ($\geq 10\mu s$) for performing Adiabatic Rapid Passage, and use a DG535 Stanford Pulse Generator to generate finer (short duration) ones for performing Rabi flopping and Ramsey interferometry. The fine or coarse pulses are then combined in an OR electronic box, whose output is sent to the TTL switch.

To prepare the atoms for Ramsey interferometry, we first apply two Adiabatic Rapid Passages, $|2,2>$ to $|1,1>$ state and then $|1,1>$ to $|2,0>$ state, to transfer all atoms from $|2,2>$ to $|2,0>$ state as shown in Figure 4.5 (a). The Ramsey interferometry process operates with microwave pulses on the $|2,0>$ to $|1,0>$ transition,

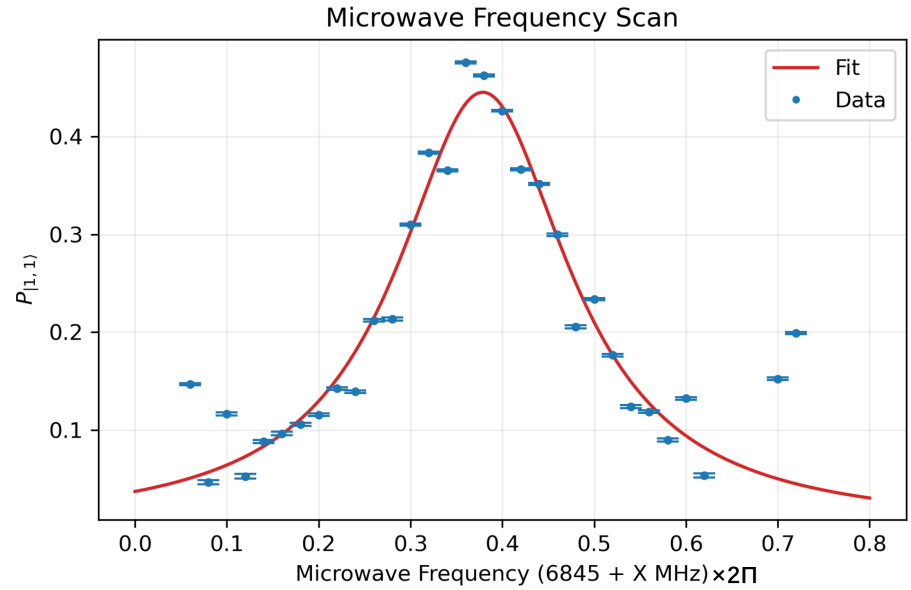

Figure 4.3: $|2,2>$ to $|1,1>$ resonance frequency scan, and the y-axis represents the population ratio of atoms in the $|1,1>$ state to the total population ratio. The fitting function is based on the Lorentzian distribution $L(x) = \frac{a}{\pi}\frac{\gamma/2}{(x-x_0)^2+(\gamma/2)^2} + b$

which is magnetically insensitive. In the atom chip region, we use a Stern-Gerlach magnetic field gradient to spatially separate atoms in different magnetic states, but it cannot directly separate $|2,0>$ and $|1,0>$ states due to their magnetic insensitivity. To achieve spatial separation, we perform another Adiabatic Rapid Passage to transfer $|2,0>$ to $|1,1>$ and $|1,0>$ to $|2,1>$ simultaneously; these two states have opposite magnetic moments. The visual demonstrations in Figure 4.4, and the logical diagram are in Figure 4.5. We note that since the $|2,0>$ and $|1,1>$, and $|1,0>$ and $|2,1>$ transitions are degenerate in our case, they can be driven simultaneously by the same microwave field (see Figure 4.5 (b)).

4.1.3 Rabi flopping and Ramsey Interferometry results

The Rabi flopping is performed by a Stanford DG535 Pulse Generator, and the on-resonance flopping diagram is shown in Figure 4.6. Based on the image, one actual

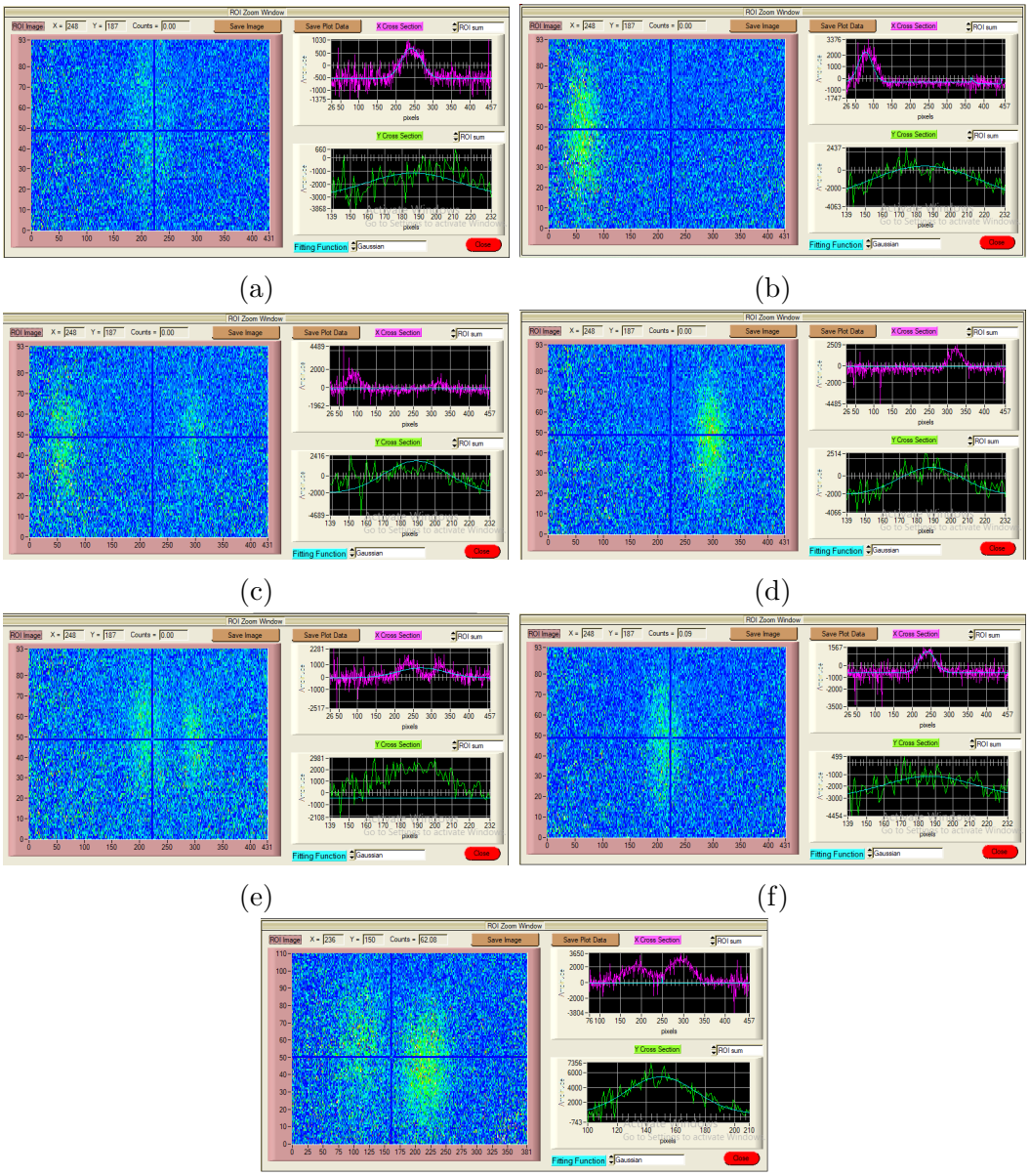

Figure 4.4: Atomic states separation demonstration with the Stern-Gerlach field with imaging by a CCD camera: (a) $|2,2>$ state without the Stern-Gerlach field, (b) $|2,2>$ state with the Stern-Gerlach field, (c) The superposition of $|2,2>$ and $|1,1>$ state with the Stern-Gerlach field, (d) Pure $|1,1>$ state with the Stern-Gerlach field, (e) The superposition of $|1,1>$ and $|2,0>$ state with the Stern-Gerlach field, (f) Pure $|2,0>$ state with the Stern-Gerlach field, (g) The superposition of $|2,0>$ and $|1,0>$ state but imaged in $|1,1>$ and $|2,1>$ state with the Stern-Gerlach field.

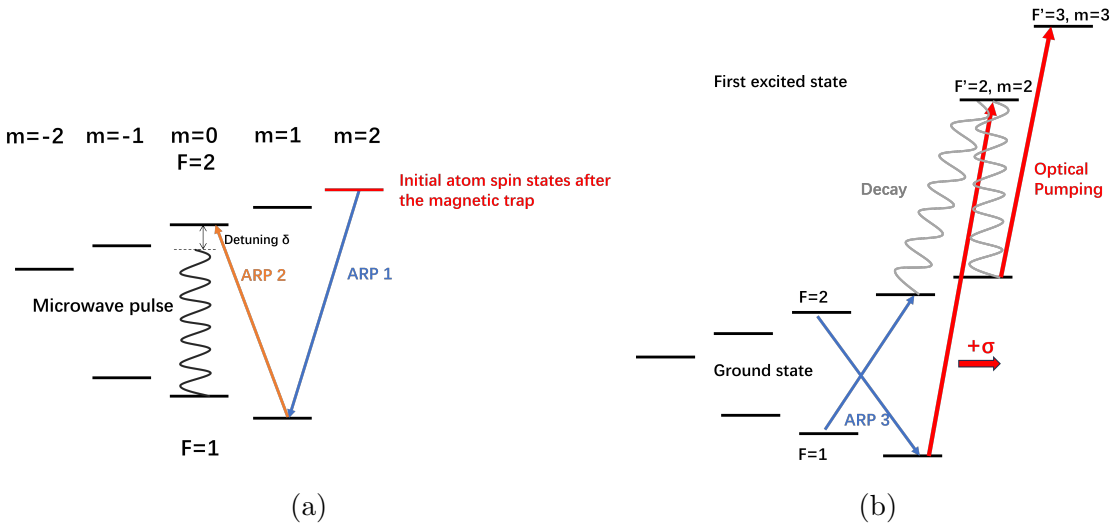

Figure 4.5: Adiabatic Rapid Passage for atomic state manipulations: (a) Preparing atoms in the $|2,0>$ state to provide a solution to create a superposition between $|2,0>$ and $|1,0>$ states, (b) Transfer atoms from $|2,0>$ and $|1,0>$ states to magnetic-sensitive states during the imaging process.

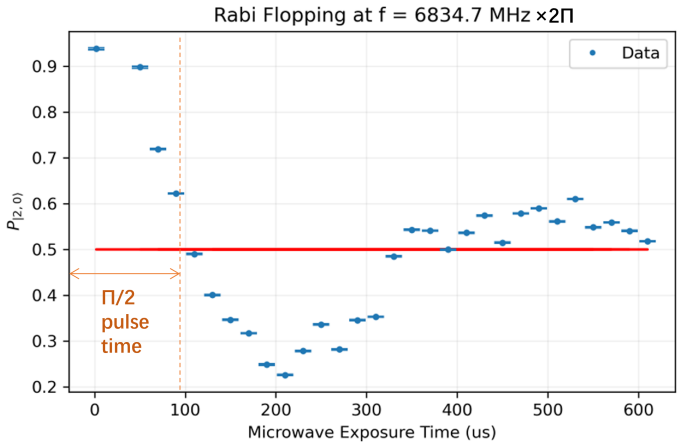

Figure 4.6: $|2,0>$ to $|1,0>$ on-resonance Rabi flopping. Note that the y-axis represents the state population ratio between atoms in the $|2,0>$ state and the total atom number in the $|2,0>$ and $|1,0>$ states.

Rabi flopping cycle is around 460 μs, which means the Rabi frequency is around is around $2\pi\times$ 2.2 kHz and the $\pi/2$ time is around 100 μs on resonance. The relatively quick decay is most likely due to the spatially inhomogeneous microwave field amplitude during a relatively long microwave exposure time.

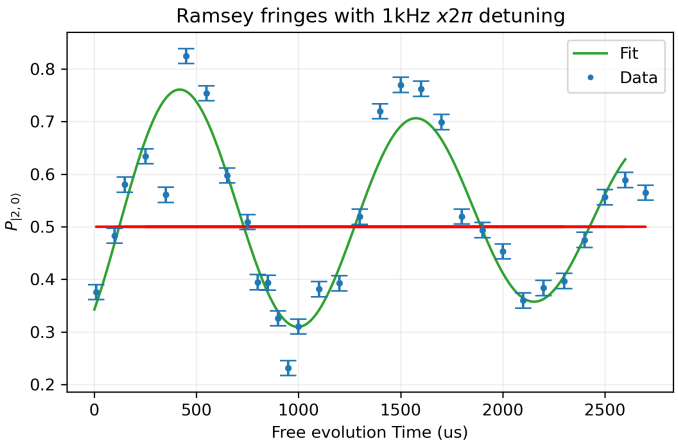

(a)

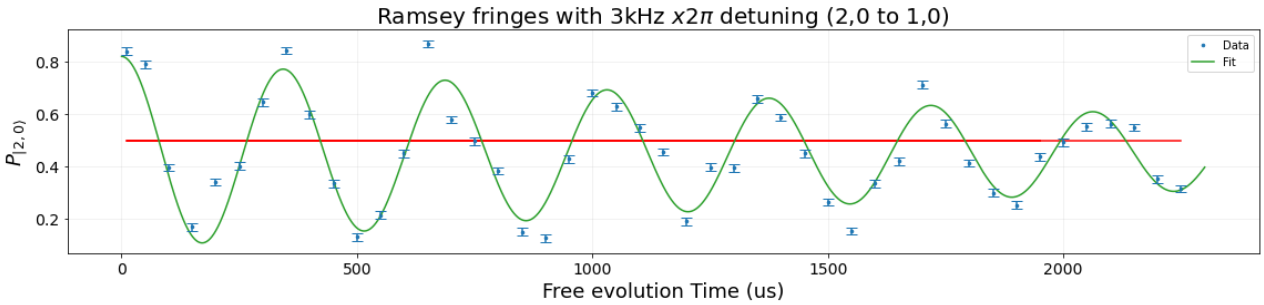

(b)

Figure 4.7: Ramsey Interferometry between $|2,0>$ and $|1,0>$ states in the ground state of Rb-87: (a) "$2\pi\times$ 1 kHz" detuning and the fitting frequency is $2\pi\times$ (0.865 $\pm$ 0.015 kHz), (b) "$2\pi\times$ 3 kHz" detuning and the fitting frequency is $2\pi\times$ (2.909 $\pm$ 0.018 kHz). Note that the y-axis represents the atomic state population ratio between atoms in the $|2,0>$ state and the total atom number in the $|2,0>$ and $|1,0>$ states. The fitting function is $F(x) = \frac{1}{2}(1 + e^{-ax}cos(bx + c))$

The Ramsey interferometry is performed with a $2\pi\times$ 1 kHz and a $2\pi\times$ 3 kHz detuning from the resonance, as shown in Figure 4.7. Based on the observed Ramsey fringes, the decoherence effect is small compared to the decoherence effect during the Rabi flopping. Because the CCD can only capture atomic clouds for around 15 ms of free fall, we cannot trace the entire Ramsey fringes until complete decoherence, but we estimate the coherence time to be around 4 ms. We can also observe that the oscillation frequency of the Ramsey fringes is around $2\pi\times$ 3 kHz or $2\pi\times$ 1 kHz, which

is given by how much the microwave is detuned from the resonance. The maximum detuning that can still create a visible $\pi/2$ pulse is around $2\pi\times$ 3.5 kHz.

4.1.4 Atomic state Population Ratio Noise

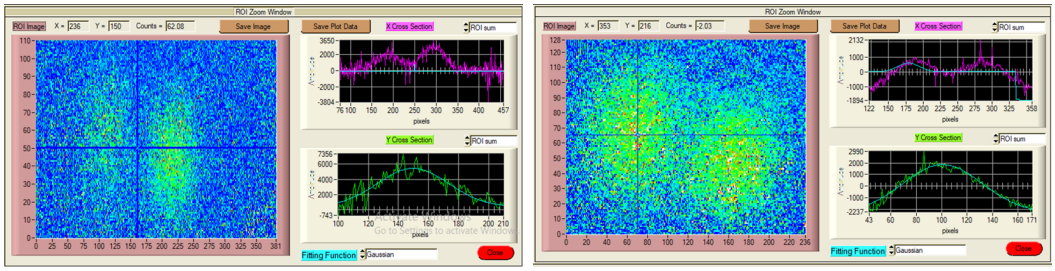

(a) (b)

Figure 4.8: Atomic noise comparison: (a) Original atomic noise; (b) Getting less atomic noise by increasing the laser power and decreasing the camera gain

The error bars are determined by the standard deviation between multiple imaging shots. All the data shown here is collected by absorption imaging. We did some improvements to reduce noise before actually collecting the data. The ROI sum of the photon counts from the camera in Figure 4.4 is very noisy, and we decrease the noise in the following manner: we reduce the noise by increasing the laser power and decreasing the camera gain to have more contrast (Figure 4.8).

Chapter 2 has discussed the first-order Zeeman splitting due to the magnetic field. Therefore, the experiment that uses the $|2,0>$ to $|1,0>$ transition is less sensitive to the ambient magnetic field than other microwave transitions, e.g., $|2,2>$ to $|1,1>$, leading to much noisier data. To be more visual, I compare the standard deviation of the atomic state ratio before and after the improvement. Figure 4.9 (a) shows the Ramsey Interferometry we attempt to perform between the $|2,2>$ and $|1,1>$ states, and the data scatter around a 10% population ratio. However, Figure 4.9(b) shows a $\pi/2$ time measurement for performing Ramsey Interferometry between the $|2,0>$ and $|1,0>$ states under a $2\pi\times$ 1 kHz detuning, and the data scatter around 5% of

the population ratio.

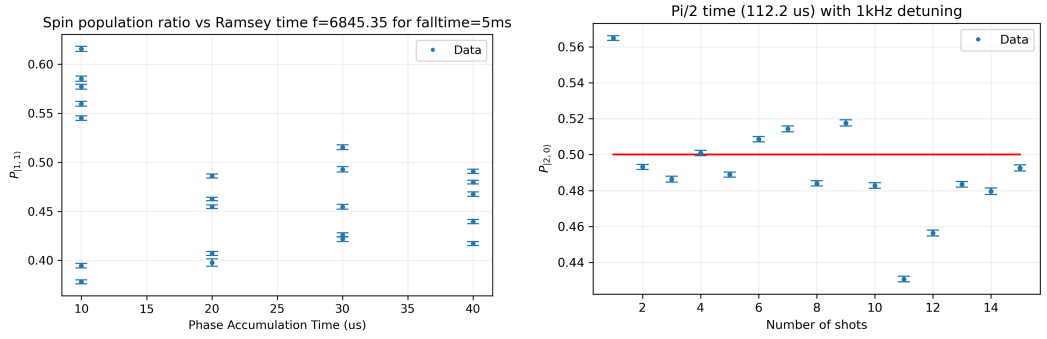

(a) (b)

Figure 4.9: Atomic noise comparison: (a) Ramsey Interferometry data between $|2,2>$ to $|1,1>$ states before the adjustment, (b) $\pi/2$ time measurement for transfer atoms from $|2,0>$ to $|1,0>$ states at 1 kHz $\times 2\pi$ detuning after the adjustment.

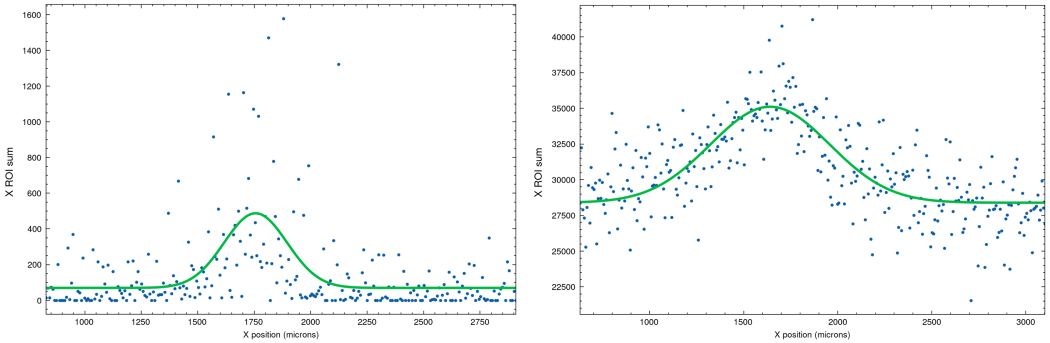

(a) (b)

Figure 4.10:
Fluorescence imaging result on the atom chip: These two figures both represent the total population of the atoms just left the chip trap. (a) has very low background light, but photon counts are discrete, and (b) has high background light and the signal is in the normal distribution. The fitting function follows the Gaussian distribution $G(x) = a\ exp(-\frac{(x-b)^2}{2c^2}) + d$

One of the goals of performing an experiment on the atom chip is to reach atomic shot noise, and an approximately 5% standard deviation in the population ratio is obviously not enough. Fluorescence imaging should yield lower atomic noise in a low-background environment, but in practice, as shown in Figure 4.10 (a), the result

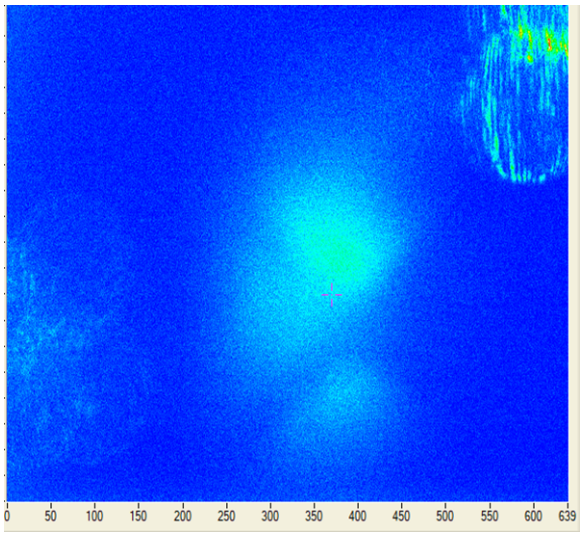

Figure 4.11: The atom cloud with an unknown magnetic gradient
Appendix provides a more concrete visualization of how the structure of the atom cloud changed during the resonance scan under the effect of a magnetic gradient.

does not look as good as we expect in a low-background environment. Next, we use a flashlight to increase the background light significantly, which gives a more uniform distribution of photon counts, as shown in Figure 4.10(b). Apparently, the photon counts are in a discrete distribution, which means the camera loses a lot of photon information if the photon counts are below the threshold for 1 digital photon count. Also, the signal is overall weak, which means the imaging laser does not have sufficient power. These results indicate that we should use a photodiode or a CCD with higher quantum efficiency to image the atoms, and also increase the fluorescence probe laser power from approximately 300 μW to at least 2 mW, possibly via a fiber amplifier.

4.2 Ramsey Interferometry Process in the MOT for imaging a laser beam

This section will focus on applying the state manipulation and Ramsey interferometry techniques developed in the previous sections (using the atom chip) to atoms in the MOT chamber with the ultimate goal of achieving Ramsey imaging of a laser beam

(though not yet achieved). Techniques similar to those used at the atom chip will also be discussed in this section.

4.2.1 Evaporation cooling

One potential issue for many ultracold experiments is the effect of unwanted magnetic gradients on the atom cloud. In this case, the atom cloud will slowly decohere and separate (Figure 4.11). Since the magnetic gradient varies with position, one good solution is to reduce the spatial extent (and expansion velocity) of the atom cloud by evaporative cooling, so that almost all parts of the cloud experience a similar magnetic field.

According to the Maxwell-Boltzmann distribution, particles at a given temperature have an energy distribution. Evaporative cooling removes high-energy particles, allowing the remaining particles to rethermalize to a lower temperature. After repeating this process many times, the cloud contains only particles with low energy, and the temperature can reach the μK-to-nK scale.

In practice, since the magnetic trap in the MOT region is a quadrupole trap, it only traps low-field-seeking atomic states. Therefore, evaporation consists of transferring the atoms in $|2,2>$ to the anti-trapped $|1,1>$ state. When implementing evaporation using a microwave signal generator, we note that a single frequency sweep is a combination of many small step functions. By properly setting the sweep range, a slow downward frequency sweep will progressively remove the most energetic atoms, thereby cooling the cloud. Importantly, setting the sweeping time long enough to extend each step-changing time allows the atomic cloud sufficient time to rethermalize.

In the experiment, we use a 3 G magnetic field to define the Zeeman splitting. Next, we applied a frequency sweep from $2\pi\times$ 20 MHz detuning above the $|2,2>$ to $|1,1>$ resonance frequency to $2\pi\times$ 2 MHz detuning in 15 seconds, and successfully

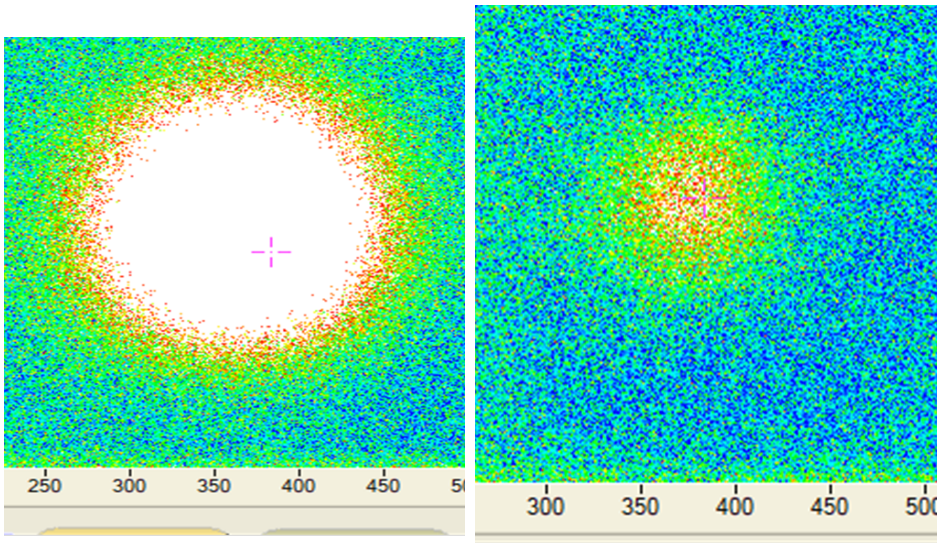

(a) (b)

Figure 4.12: (a) Atom cloud before the evaporation cooling (b) Atom cloud after the evaporation cooling.

created a cloud with $12.587 \pm 0.041\ \mu K$ (Figures 4.12 and 4.13). However, our goal is not to make the cloud colder but only to make it sufficiently compact, so we usually use atom clouds with a temperature higher than this to obtain an adequate atom population for a good imaging signal. In our later experiment, we prefer a frequency sweep over a range of around $2\pi\times$ 15 MHz in 10 seconds, ending at around $2\pi\times$ 4 MHz away from the $|2,2>$ to $|1,1>$ resonance frequency.

4.2.2 Resonance scans of microwave transitions and corresponding Rabi flopping

Next, we turn off all magnetic traps and let the atoms free-fall to perform Ramsey Interferometry. Effective mitigation of the magnetic gradient effect on an atom cloud enables microwave operations on the cloud, such as atomic state manipulations. We prefer to use a relatively strong background magnetic field to define the quantization axis and reduce the effect of unknown magnetic gradients. In our case, we use 7.5 G for the MOT region, so then the frequency gap between nearby m_F levels is $2\pi\times$ 5.35

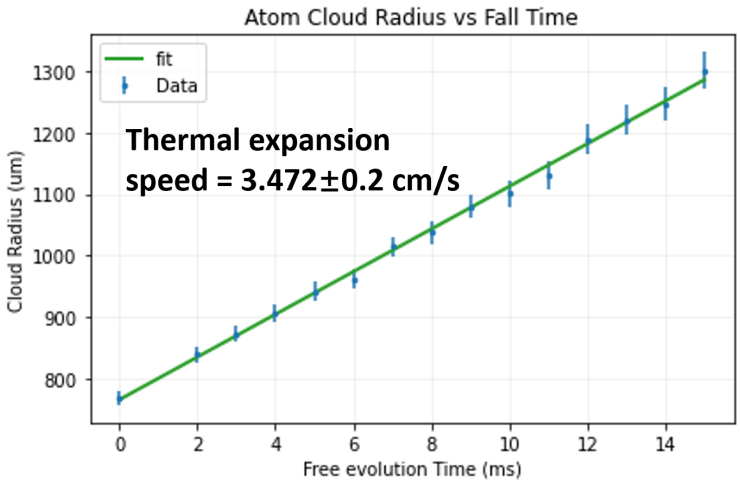

Figure 4.13: Thermal expansion rate of an atom cloud after the evaporation cooling The thermal expansion speed is 3.472 ± 0.2 cm/s. The x-axis is the free-fall expansion time (i.e., time-of-flight), and the y-axis is the diameter of the atom cloud in μm. The fitting function is a linear line $y = ax + b$, where a is the expansion velocity.

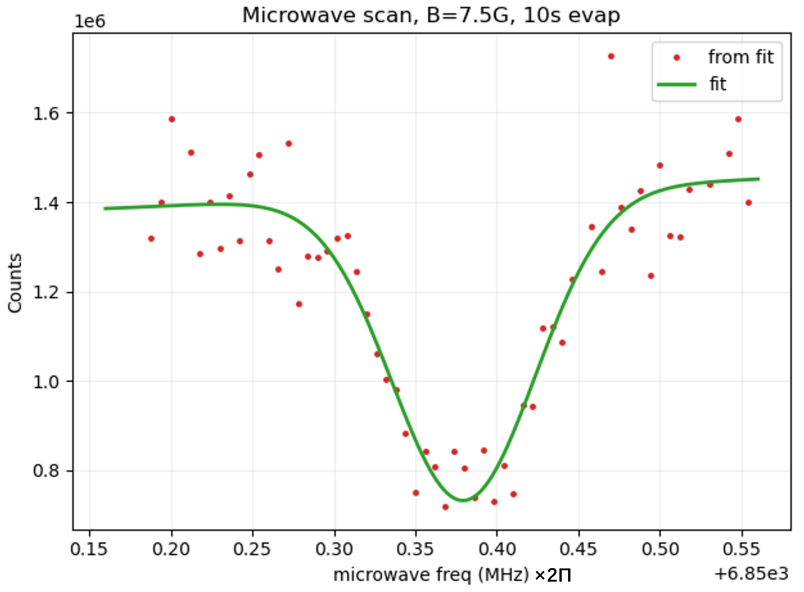

Figure 4.14: $|2, 2>$ to $|1, 1>$ resonance scan under 7.5 G vertical bias field in the MOT region. Resonance frequency = $2\pi\times$ (6850.38 ± 0.003 MHz). The fitting function follows the Gaussian distribution $G(x) = a\ exp(-\frac{(x-b)^2}{2c^2}) + d$.

MHz.

Similar to the work on the atom chip region, we scan the $|2,2>$ to $|1,1>$ resonance in the MOT region, and the result is shown below in Figure 4.14. By fitting the resonance with a Gaussian, we find a width of around $2\pi\times$ (87.764 $\pm$ 6.528 kHz), and a central resonance frequency at around $2\pi\times$ (6850.38 $\pm$ 0.003 MHz).

Based on this frequency, we perform Rabi flopping on or near the resonance. The results are shown in Figure 4.15. An interesting thing is that only around 25% of the atom population is undergoing Rabi flopping. A pure set of data is recorded at a $2\pi\times$ 2 MHz detuning (very far detuned) from the resonance frequency, and the noise-like data points confirm that the population oscillation was driven by the microwave field. According to the Rabi flopping graph on the small and large time scales, the Rabi frequency of the atom cloud in the MOT region between the $|2,2>$ and $|1,1>$ states is around $2\pi\times$ 50 kHz, and the system starts to decohere after about 1 ms.

Based on the Rabi frequency and the resonance linewidth, we perform an ARP (Adiabatic Rapid Passage) to transfer the atoms from $|2,2>$ and $|1,1>$. We sweep a $2\pi\times$ 200 kHz range from below to above the resonance in 2 ms, and the result is shown in Figure 4.15. This ARP currently has around 70% efficiency.

Next, we performed microwave-frequency scans to search for the $|1,1>$ to $|2,0>$ resonance, and Figure 4.17 shows the scan result. Fitted resonance width is $2\pi\times$ (24.123 $\pm$ 5.721 kHz) and resonance frequency is $2\pi\times$ (6839.903 $\pm$ 0.002 MHz). The $|1,1>$ to $|2,0>$ on resonance Rabi flopping is shown in Figure 4.18 with fitted frequency $\Omega = 2\pi\times$ (8.509 $\pm$ 0.205 kHz). Based on the Rabi frequency in Figure 4.18, we perform a sweep of $2\pi\times$ 60 kHz range from below the resonance to above in 2 ms. This $|1,1>$ to $|2,0>$ Adiabatic Rapid Passage achieved around 50% population transfer efficiency (Figure 4.19). Therefore, when performing Rabi flopping or Ramsey Interferometry between the $|2,0>$ and $|1,0>$ states, only half of the atoms in the

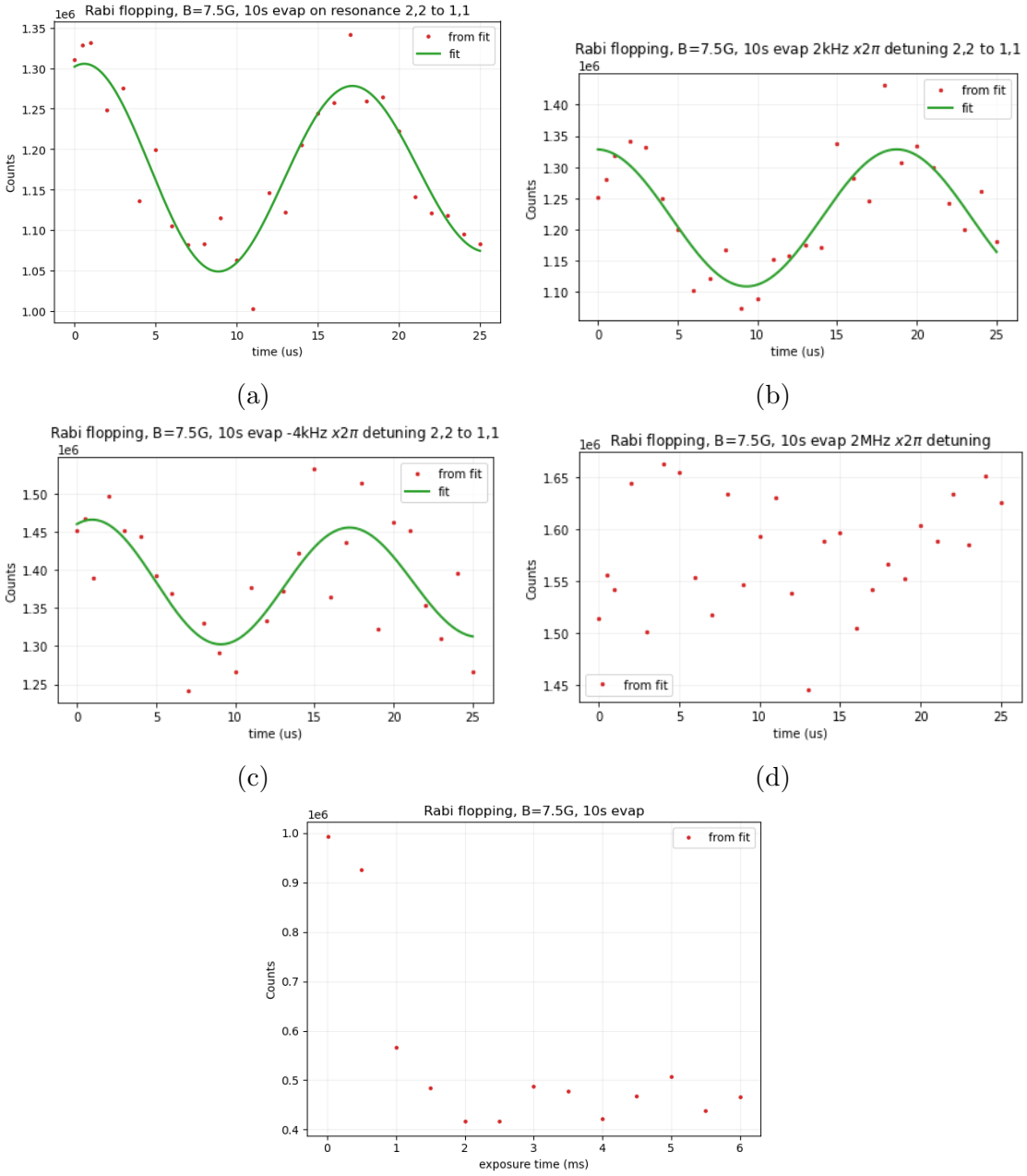

Figure 4.15: Rabi flopping between $|2,2>$ and $|1,1>$ states in the MOT region. (a) On resonance (Fitted frequency Ω= $2\pi\times$ (60.522 $\pm$ 2.183 kHz)) (b) $2\pi\times$ 2 kHz detuning (Fitted frequency Ω' =$2\pi\times$ (53.110 $\pm$ 2.618 kHz)) (c)$2\pi\times$ (-)4 kHz detuning (Fitted frequency Ω'= $2\pi\times$ (61.538 $\pm$ 4.930 kHz)) (d)$2\pi\times$ 2 MHz detuning (e) On resonance, but on a larger time scale (ms). The fitting function is $F(x) = \frac{1}{2}(a + be^{-cx}cos(dx + e))$.

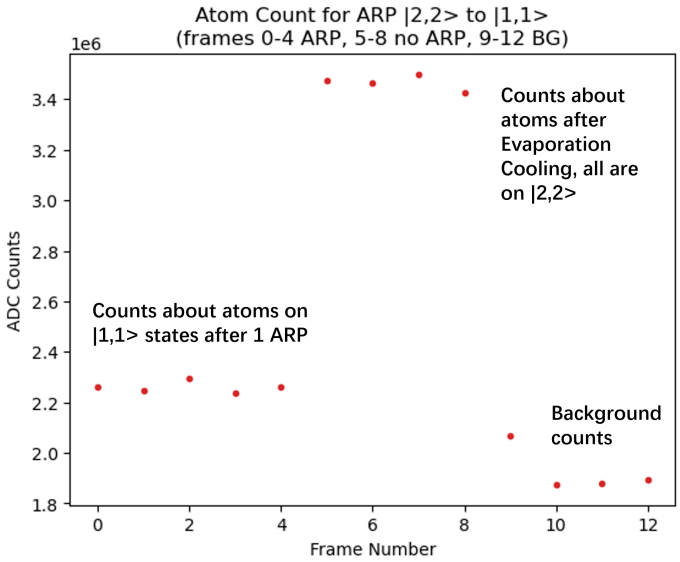

Figure 4.16: Adiabatic Rapid Passage from $|2,2>$ and $|1,1>$ states in MOT region Frame 0-4 records the F=2 atom imaging counts after performing the ARP; Frame 5-8 records the atom imaging counts without performing the ARP; Frame 9-12 records the imaging counts without the atoms (the camera only receives photons from the environment, such as room light or reflected light due to the glass cell)

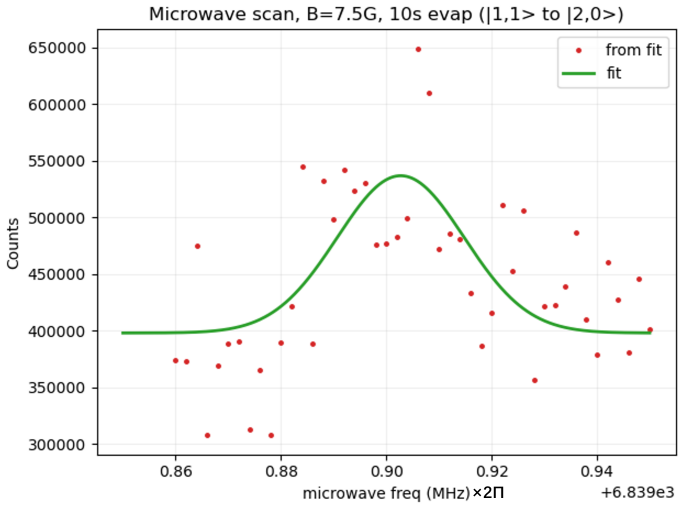

Figure 4.17: $|1,1>$ to $|2,0>$ resonance scan under 7.5 G bias field in the MOT region. Resonance frequency = $2\pi\times$ (6839.903 $\pm$ 0.002 MHz). The fitting function follows the Gaussian distribution $G(x) = a\ exp(-\frac{(x-b)^2}{2c^2}) + d$.

cloud are driven by the microwave field and participate in these measurements (the other half of the population remains in the $|2,2>$ and $|1,1>$ states, unfortunately).

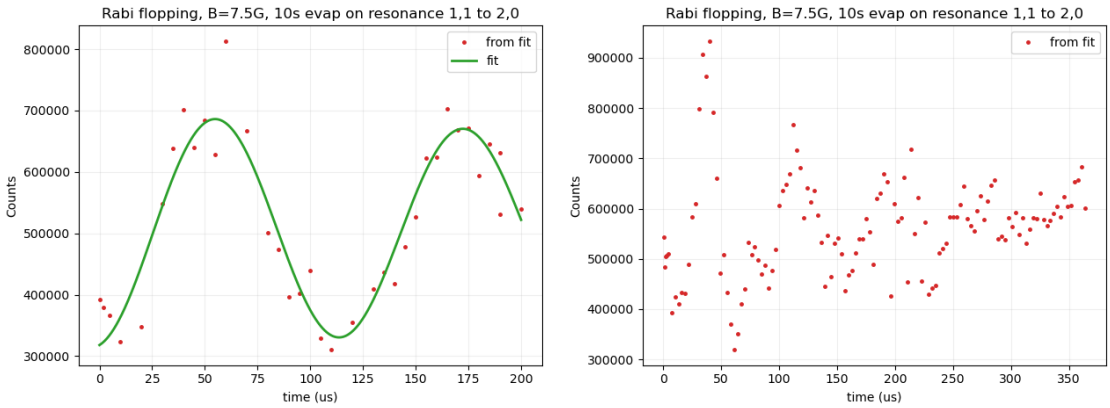

(a) (b)

Figure 4.18: $|1,1>$ to $|2,0>$ Rabi flopping with on resonance frequency under 7.5 G bias field in the MOT region: (a) shows the Rabi flopping on a shorter time scale with fit (Fitted frequency $\Omega = 2\pi\times$ (8.509 $\pm$ 0.205 kHz)); (b) shows the Rabi frequency on a longer time scale to highlight the decoherence effect. The fitting function is $F(x) = \frac{1}{2}(a + be^{-cx}cos(dx + e))$

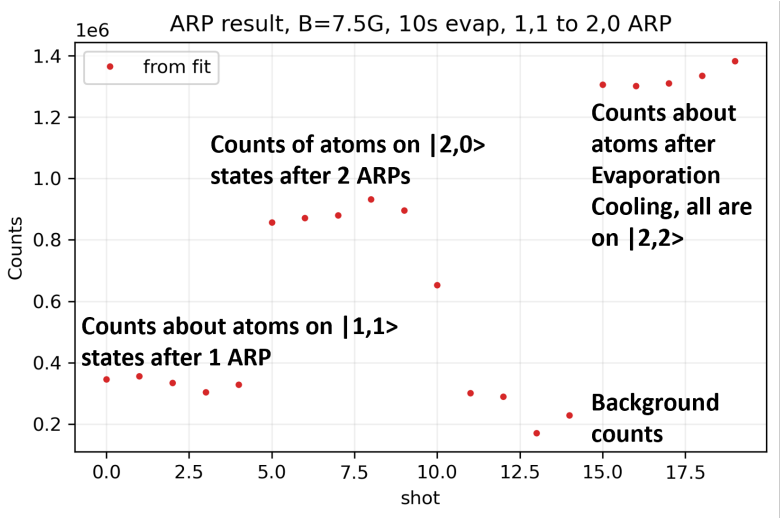

Figure 4.19: Adiabatic Rapid Passage from $|1,1>$ and $|2,0>$ states in the MOT region. Frame 0-4 records the F=2 atom imaging counts after performing the first ARP ($|2,2>$ to $|1,1>$); Frame 5-9 records the F=2 atom imaging counts after performing the first ARP ($|2,2>$ to $|1,1>$) and the second ARP ($|1,1>$ to $|2,0>$); Frame 10-14 records the imaging counts without the atoms (the camera only receives photons from the environment, such as room light or reflected light due to the glass cell); Frame 15-19 records the F=2 atom imaging counts just after the Evaporation Cooling (without any ARP).

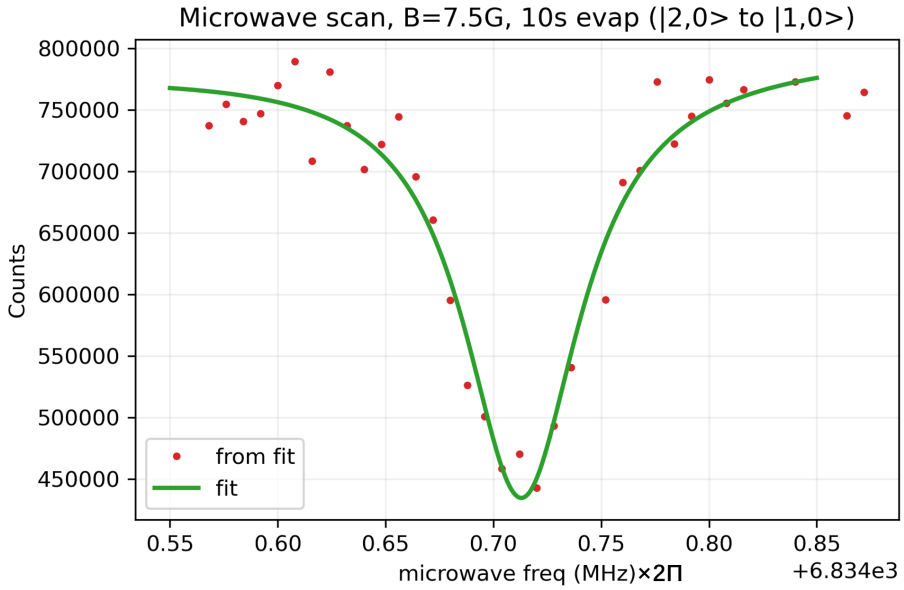

Figure 4.20: $|1,1>$ to $|2,0>$ resonance frequency scan and fitted frequency $= 2\pi\times$ (6834.713 $\pm$ 0.002 MHz). The fitting function is based on the Lorentzian distribution $L(x) = \frac{a}{\pi}\frac{\gamma/2}{(x-x_0)^2+(\gamma/2)^2} + b$.

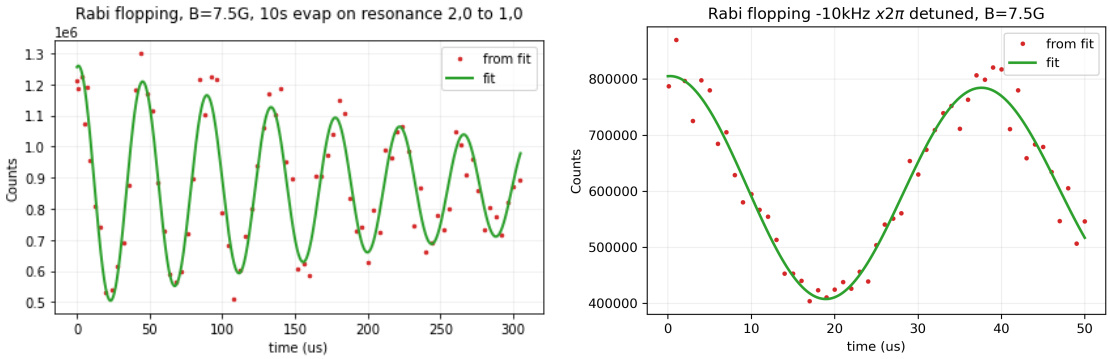

(a) (b)

Figure 4.21: $|2,0>$ to $|1,0>$ Rabi flopping under 7.5 G bias field in the MOT region (a) shows the Rabi flopping on resonance frequency with a larger time scale with fit (Fitted frequency $\Omega = 2\pi\times$ (22.643 $\pm$ 0.085 kHz)); (b) shows the Rabi frequency with $2\pi\times$ (-)10 kHz detuning in a shorter time scale to measure the $\pi/2$ time for performing Ramsey Interferometry. The fitting function is $F(x) = \frac{1}{2}(a + be^{-cx}cos(dx + e))$

The frequency scan for $|2,0>$ to $|1,0>$ transition resonance is shown in Figure 4.20. Fitted resonance frequency $= 2\pi\times$ (6834.713 $\pm$ 0.002 MHz), and the resonance

width = $2\pi\times$ (128.252 $\pm$ 18.002 kHz). The on-resonance Rabi flopping between $|2,0>$ and $|1,0>$ is shown in Figure 4.21. The suppression of decoherence by magnetic gradient and magnetic noise in the environment is easy to see by comparing the Rabi flopping between $|2,0>$ and $|1,0>$ (magnetic insensitive) in Figure 4.21 (a) and the Rabi flopping between $|2,0>$ and $|1,1>$ (magnetic sensitive) in Figure 4.18 (b).

We attempted to use a $2\pi\times$ 20 kHz detuning from the $|2,0>$ to $|1,0>$ resonance frequency, but we were not able to perform a good $\pi/2$ pulse to create a 50/50 superposition. Figure 4.21 (b) shows the Rabi flopping with a $2\pi\times$ (-)10 kHz detuning. We use the average F=2 atom imaging counts after a pure π pulse (no detuning) as a reference to see how many atoms can be transferred to the $|1,0>$ state at maximum. Based on this logic, we find that the $\pi/2$ time under a $2\pi\times$ (-)10 kHz detuning for the $|2,0>$ to $|1,0>$ transition is 14.614 $\pm$ 1 μs (the errorbar here is roughly estimated, and the photon counts fluctuation mainly contributes to this value).

4.2.3 Ramsey interferometry

Based on the $2\pi\times$ (-)10 kHz detuned driving microwave field and the $\pi/2$ time $\approx$ 14 μs, we successfully perform the Ramsey Interferometry in the MOT region between the $|2,0>$ and $|1,0>$ states (Figure 4.22). Figure 4.22 represents one of the main achievements of this section, chapter, and thesis. Based on Figure 4.22, there seems to be no decoherence in the first 1 ms free evolution time. Here we use a detuning value $2\pi\times$ (-)10 kHz, which is half of the Rabi frequency. According to Chapter 2, when the detuning value of the driving field is significant compared to the Rabi frequency, the Ramsey fringe will have $-\pi/6$ or $-5\pi/6$ phase shift. In this case, the Ramsey fringe has an around $-5\pi/6$ phase shift.

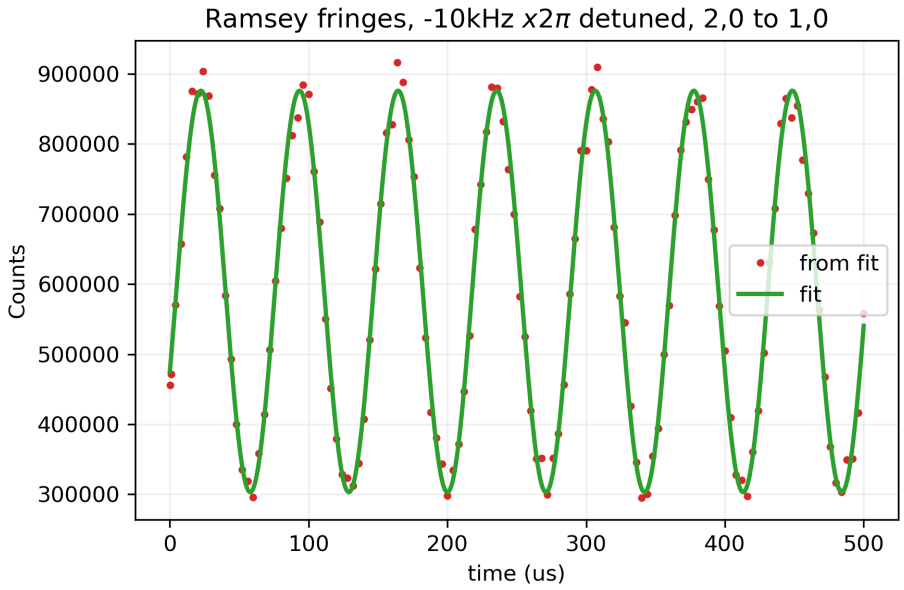

(a)

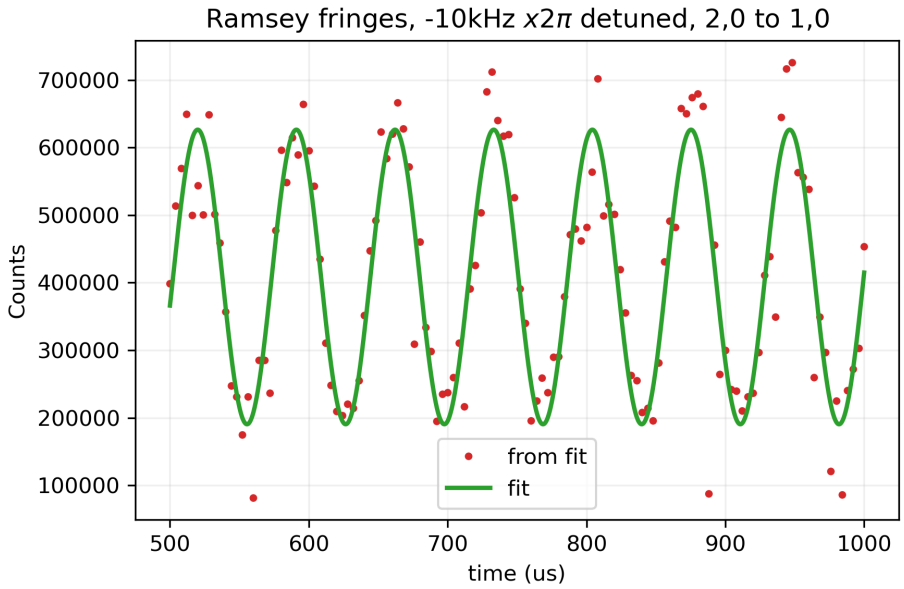

(b)

Figure 4.22: Ramsey Interferometry between $|2,0>$ and $|1,0>$ states with $2\pi\times$ (-)10kHz detuning. (a) and (b) are under different free evolution time ranges. The frequency of fringe in (a) is $2\pi\times$ (14.076 $\pm$ 0.009 kHz); the frequency of fringe in (b) is $2\pi\times$ (14.072 $\pm$ 0.044 kHz). Note that the data fluctuation in (b) is mainly caused by the unstable laser lock. The fitting function is $F(x) = \frac{1}{2}(a + be^{-cx}cos(dx + e))$

4.2.4 Prospects for Ramsey interferometry-based imaging a laser beam

We plan to implement a short laser pulse that is far detuned from any optical transition during the atoms' free evolution time. Technically, the short laser pulse in tens of μs scale will need the AOM controls (Appendix A.2). We intend to perform Ramsey Interferometry with several hundred μs (with the maximum initial coherence) to observe either the decoherence effect brought by the scattering light, or the phase shifts (fringe oscillation frequency changes) due to the AC Stark shifts.

Chapter 5

Conclusion

This thesis presents many of the techniques and details needed for the atom state manipulation by microwave field and the Ramsey Interferometry for laser-beam imaging, which was originally proposed in the introduction:

Crucially, the IQ-modulator-based microwave system provides an agile but stable microwave frequency source around $2\pi\times$ 6.8 GHz for atomic state manipulation (i.e., $\pi/2$ pulse or Adiabatic Rapid Passage).

The discussions on the current imaging system, both at the atom chip region and in the MOT region, provide conceptual and technical descriptions of how we collected the data.

The implementation of a microwave field with an antenna at the atom chip or a waveguide in the MOT region let us successfully perform evaporation cooling, Rabi flopping between Zeeman splitting levels in the Rb-87 ground levels (F=1 and F=2), multiple Adiabatic Rapid Passages to transfer the atoms to magnetically insensitive levels, and finally Ramsey Interferometry.

Outlook

There are some ideas for possible next steps in these experiments:

1) For a part of the future plan, since the second-order effect on energy levels by a magnetic gradient has been discussed several times, it will be good to perform the

Spin Echo (discussed in Chapter 2), which is more tolerant to the magnetic gradient in the environment (not varying in a short time).

2) Additionally, since Ramsey Interferometry has been successful, it will be great to proceed with imaging a laser beam in the MOT in the future (Some preliminary works are shown in Appendix A.2).

3) Currently, since the Adiabatic Rapid Passages didn't fully transfer the atoms from $F = 2, m = 2$ to $F = 2, m = 0$ in the MOT region, the experimental Ramsey fringe contrast is not good enough. It will be reasonable to develop techniques either to purify the states during the data collection or to make state transfer more efficient.

4) The result section discusses the noise for analyzing the atomic population or ratio. Minimizing noise will also be one of the most important goals, and hopefully, we can reach atomic shot noise on the atom chip by implementing the new imaging system (discussed in Appendix A.3).

Appendix A

A.1 The atom cloud structure during a resonance scan under a magnetic gradient

The figures (a) to (h) represent the atom cloud structures when being coupled by a microwave starting from a frequency below the resonance frequency, scanning across the resonance, and ending with the frequency above the resonance frequency.

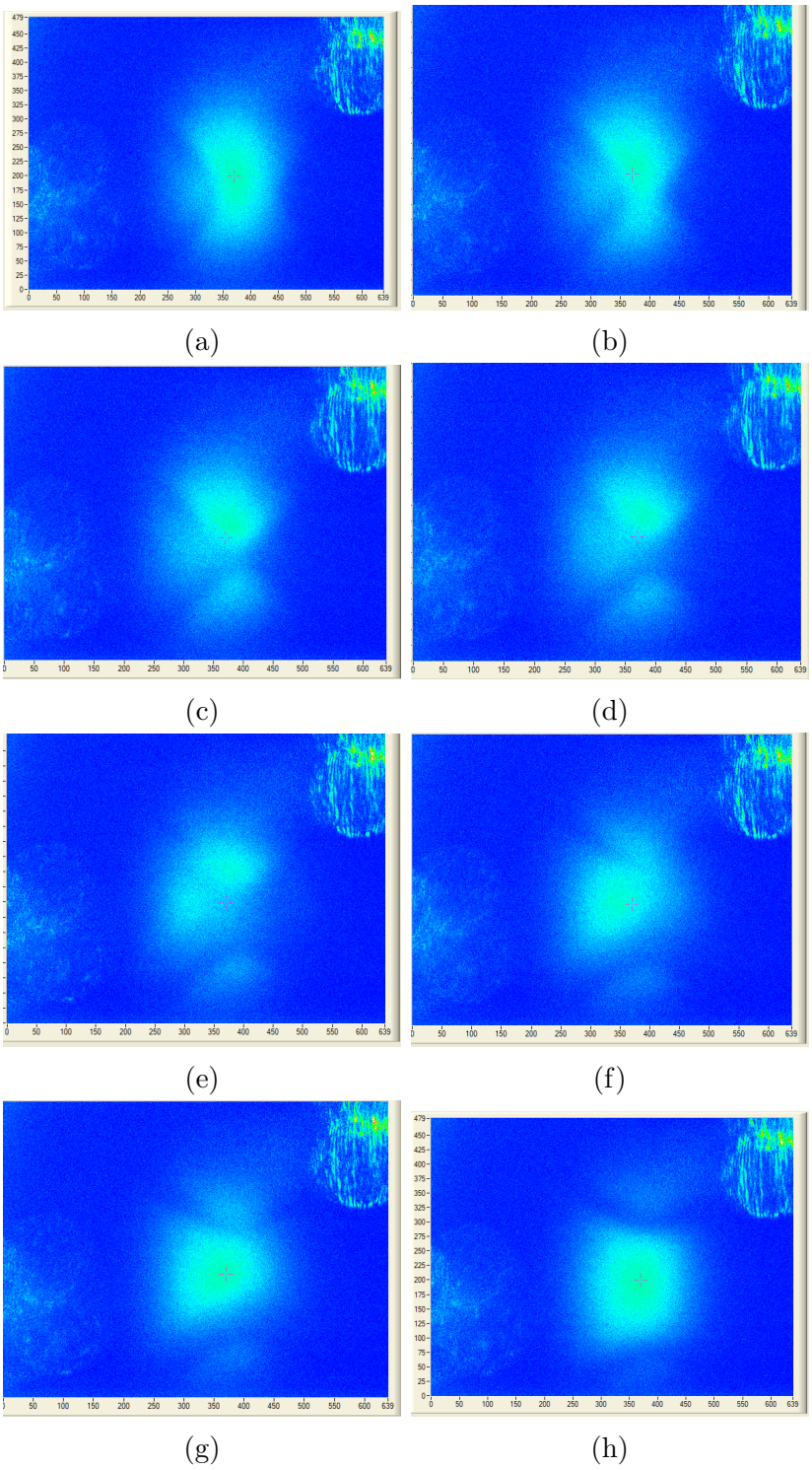

Figure A.1: Atom cloud structures during the resonance scan under the effect of an unknown external magnetic gradient

A.2 Pre-works for imaging a laser beam

Figure A.2 describes the AOM (Acousto-optic modulator) system for providing a μs scale laser pulse.

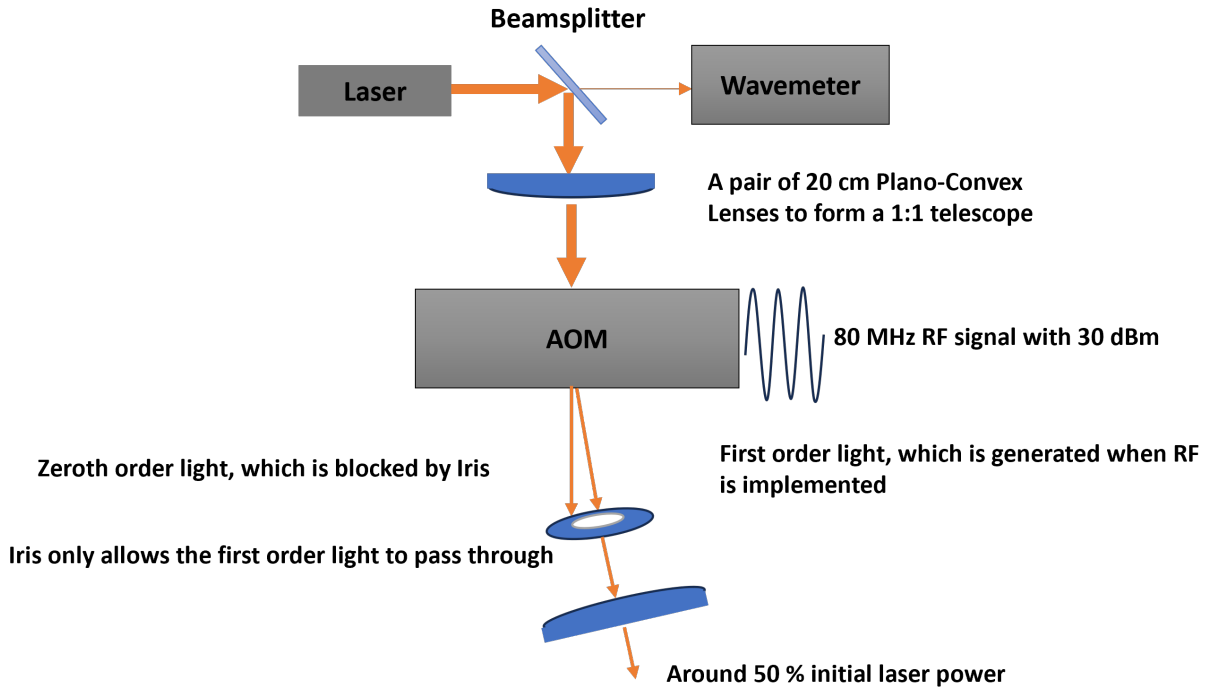

Figure A.2: We intend to send the first-order light, after passing through the AOM (which will be around 80 MHz higher than the original laser frequency), to the MOT region. The wavemeter is attached to monitor the laser frequency.

A.3 New version of fluorescence imaging system

To collect less noisy data, we want to maximize the target signal and minimize environmental noise. The system shown below (Figure A.3) is designed to isolate environmental noise. Later, at the atom chip region, we may increase the target experimental signal by increasing the imaging laser power.

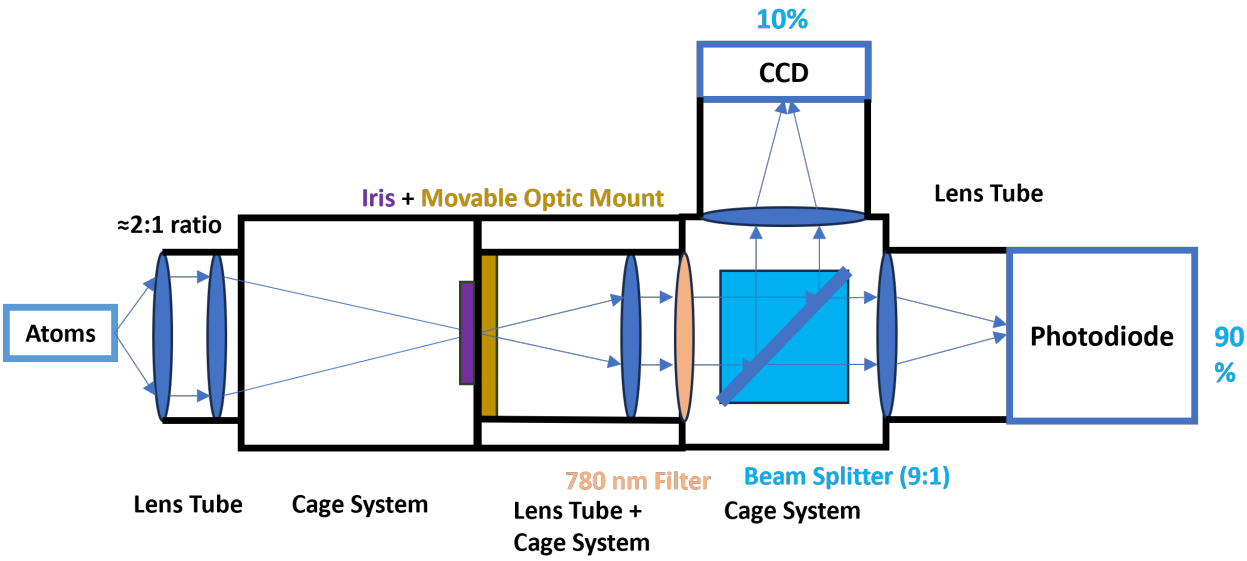

Figure A.3: We use a combination of lens tubes and cage systems to minimize environmental noise, and we add an iris in the middle to block unexpected signals from the reflected imaging beam or environmental light. We will mainly rely on the photodiode to collect data. The CCD will be used for aligning the system.

References

[1] Akio Kawasaki. "Tracking a nonrelativistic charge with an array of Rydberg atoms". In: *Phys. Rev. Res.* 5 (4 Nov. 2023), p. 043178. DOI: 10.1103/PhysRevResearch.5.043178. URL: https://link.aps.org/doi/10.1103/PhysRevResearch.5.043178.

[2] Nicolas DeStefano et al. "Electron beam characterization via quantum coherent optical magnetometry". In: *Applied Physics Letters* 125.26 (Dec. 2024), p. 264001. ISSN: 0003-6951. DOI: 10.1063/5.0234219. eprint: https://pubs.aip.org/aip/apl/article-pdf/doi/10.1063/5.0234219/20315793/264001_1_5.0234219.pdf. URL: https://doi.org/10.1063/5.0234219.

[3] Noah Schlossberger et al. "Two-dimensional imaging of electromagnetic fields via light-sheetfluorescence imaging with Rydberg atoms". In: *Opt. Lett.* 50.23 (Dec. 2025), pp. 7312–7315. DOI: 10.1364/OL.566697. URL: https://opg.optica.org/ol/abstract.cfm?URI=ol-50-23-7312.

[4] Daniel A. Steck. *Rubidium 87 D Line Data*. https://steck.us/alkalidata/rubidium87numbers.1.6.pdf. [Accessed 16-04-2026]. 14 October 2003.

[5] V. A. Yerokhin et al. "Electric dipole polarizabilities of Rydberg states of alkali-metal atoms". In: *Phys. Rev. A* 94 (3 Sept. 2016), p. 032503. DOI: 10.1103/PhysRevA.94.032503. URL: https://link.aps.org/doi/10.1103/PhysRevA.94.032503.

[6] Saeed Pegahan et al. "Development of a Rydberg Atom-Based Apparatus for Tracking Charged Particles". In: *APS Division of Atomic, Molecular and Optical Physics Meeting Abstracts*. Vol. 2023. APS Meeting Abstracts. Jan. 2023, F02.009, F02.009.

[7] Megan K. Ivory. "Experimental Apparatus for Quantum Pumping with a Bose-Einstein Condensate". PhD thesis. William & Mary, 2016. DOI: 10.21220/m2-4bwj-8856. URL: https://dx.doi.org/doi:10.21220/m2-4bwj-8856.

[8] Austin R. Ziltz. "Ultracold rubidium and potassium system for atom chip-based microwave and RF potentials". PhD thesis. William & Mary, 2015. DOI: 10.21220/s2-rejy-4083. URL: https://dx.doi.org/doi:10.21220/s2-rejy-4083.